A superconducting gravimeter on the island of Heligoland for the high-accuracy determination of regional ocean tide loading signals of the North Sea

Christian Voigt [1], Roman Sulzbach,[1,2] Ludger Timmen,[3] Henryk Dobslaw [1],
Adelheid Weise,[3] Zhiguo Deng,[1] Nico Stolarczuk,[1] Hartmut Pflug,[1] Heino Peters,[4]
Michael Fietz,[4] Maik Thomas,[1,2] Christoph Förste[1] and Frank Flechtner[1,5]

[1]*Department Geodesy, Helmholtz Centre Potsdam - GFZ German Research Centre for Geosciences, Telegrafenberg,* 14473 *Potsdam, Germany.*
E-mail: *christian.voigt@gfz-potsdam.de*
[2]*Institute of Meteorology, Freie Universität Berlin (FUB), Carl-Heinrich-Becker-Weg* 6-10, 12165 *Berlin, Germany*
[3]*Institute of Geodesy, Leibniz Universität Hannover (LUH), Schneiderberg* 50, 30167 *Hannover, Germany*
[4]*Biologische Anstalt Helgoland, Alfred-Wegener-Institute (AWI), Helmholtz Centre for Polar and Marine Research, Ostkaje* 1118, 27498 *Helgoland, Germany*
[5]*Institute of Geodesy and Geoinformation Science, Technische Universität Berlin (TUB), Kaiserin-Augusta-Allee* 104-106, 10553 *Berlin, Germany*

SUMMARY

The superconducting gravimeter GWR iGrav 047 has been installed on the small offshore island of Heligoland in the North Sea approximately at sea level with the overall aim of high-accuracy determination of regional tidal and non-tidal ocean loading signals. For validation, a second gravimeter (gPhoneX 152) has been setup within a gravity gradiometer approach to observe temporal gravity variations in parallel on the upper land of Heligoland. This study covers the determination of regional ocean tide loading (OTL) parameters based on the two continuous gravimetric time-series after elimination of the height-dependent gravity component by empirical transfer functions between the local sea level from a nearby tide gauge and local attraction effects. After reduction of all gravity recordings to sea level, both gravimeters provide very similar height-independent OTL parameters for the eight major diurnal and semidiurnal waves with estimated amplitudes between 0.3 nm s^{-2} (Q$_1$) and 11 nm s^{-2} (M$_2$) and RMSE of 0.1–0.2 nm s^{-2} for 2 yr of iGrav 047 observations and a factor of 2 worse for 1.5 yr of gPhoneX 152 observations. The mean absolute OTL amplitude differences are 0.3 nm s^{-2} between iGrav 047 and gPhoneX 152, 0.4 nm s^{-2} between iGrav 047 and the ocean tide model FES2014b and 0.7 nm s^{-2} between gPhoneX 152 and FES2014b which is in good agreement with the uncertainty estimations. As by-product of this study, OTL vertical displacements are estimated from the height-independent OTL gravity results from iGrav 047 applying proportionality factors dh/dg for the eight major waves. These height-to-gravity ratios and the corresponding phase shifts are derived from FES2014b. The OTL vertical displacements from iGrav 047 are estimated with amplitudes between 0.4 mm (Q1) and 5.1 mm (M2) and RMSE of 0.1–0.7 mm. These OTL amplitudes agree with FES2014b within 0.0 (M2) and 0.8 mm (K1) with a mean difference of 0.3 mm only. The OTL amplitudes from almost 5 yr of GNSS observations show deviations of up to 6 mm (M$_2$) compared to vertical displacements from both iGrav 047 and FES2014b, which suggests systematic effects included in the estimation of OTL vertical displacements from GNSS. With the demonstrated accuracy, height-independent sensitivity in terms of gravity and vertical displacements along with the high temporal resolution and the even better performance with length of time-series, iGrav 047 delivers the best observational signal for OTL which is representative for a large part of the North Sea.

Key words: Loading of the Earth; Tides and planetary waves; Time variable gravity.

1 INTRODUCTION

The direct mass attraction from the astronomical bodies Sun and Moon induce solid Earth tides that provide the largest contribution to gravimetric observations. Besides, near-coastal gravimetric observations are primarily influenced by tidal and non-tidal ocean loading signals including a large contribution from the direct Newtonian attraction of the nearby sea masses. With increasing distance to the coast, significant tidal and non-tidal ocean loading signals still affect gravimetric time-series due to the varying water mass load on the Earth's crust as well as the corresponding vertical displacement of the sea floor and the continental topographic surface. The ocean tide loading (OTL) signals, generally not in phase with the solid Earth tides, are best estimated on the basis of multiyear time-series at continuously operating stations by local tidal analyses, see, for example Sulzbach *et al.* (2022) as recent example for the estimation of degree-3 OTL signals by long-term superconducting gravimeter (SG) time-series. Non-tidal ocean loading signals are generally much smaller in amplitude except during isolated extreme events, but they are nevertheless a significant source of geophysically induced noise in terrestrial gravimetry aiming at uncertainties of 10 $nm\,s^{-2}$ and less (Hinderer *et al.* 2015; Van Camp *et al.* 2017). However, the estimation of non-tidal ocean loading signals far away from the coast suffers from small amplitudes and interferences with unknown local signals, primarily terrestrial water storage variations (groundwater storage and soil moisture variations) typically exceeding by far non-tidal ocean loading signals of maximum 5–10 $nm\,s^{-2}$ on SG stations several 100 km away from the coast (Fratepietro *et al.* 2006; Boy & Lyard 2008). On the other hand, near-coastal gravimeter setups are usually avoided due to enhanced observation noise and significant signals from local sea mass variations.

The overall aim of the Heligoland study site (Fig. 1) is the high-accuracy estimation of regional tidal and non-tidal ocean loading signals of the North Sea based on a SG record. The small offshore island of Heligoland in the North Sea is chosen for the installation in order to increase the signal-to-noise ratio and to reduce the interferences with terrestrial water storage variations. Heligoland (German: Helgoland) is located 50 km away from the mainland and covers an area of 1.7 km^2. The topography of Heligoland is divided into a lower and an upper land which allows for a gravity gradiometer setup at significantly different heights. In addition, there are already redundantly operating sensors like tide gauges and GNSS available. As the local signals on the island of Heligoland are far more homogeneous and better observed by local tide gauges than underground water storage variations on the mainland, the derivation of regional tidal and non-tidal ocean loading signals is targeted, in the best case representative for the German Bight in the North Sea covering an area of 77 000 km^2 along the Danish–German–Dutch coast. The SG-based regional non-tidal and tidal ocean loading signals are expected to be of highest accuracy and will serve as 'ground truth' for the calibration and validation of recent and future ocean tide models, of satellite gravimetry from GRACE Follow-On (Landerer *et al.* 2020) and corresponding de-aliasing products AOD1B RL06 (Dobslaw *et al.* 2017) as well as for supporting optical clock comparisons between height benchmarks on the mainland and the island of Heligoland at the level of 10^{-18} (Voigt *et al.* 2016a). Finally, the SG network in Central Europe will strongly benefit from an improved knowledge of non-tidal ocean loading signals of the North Sea.

First gravimetric analyses at Heligoland were done by Weise *et al.* (2020) on tidal and non-tidal ocean loading observations from three continuously operating spring gravimeters (ZLS B64, Scintrex CG5-211 and CG6-49) during the winter period 2018–2019 including tidal analyses with amplitude differences within 1 $nm\,s^{-2}$ between side-by-side observing gravimeters ZLS and CG6. In addition, they show that non-tidal ocean loading signals can reach amplitudes of up to 120 $nm\,s^{-2}$ and −20 mm in terms of gravity and vertical displacements, respectively, during storm surges with 1.7 m above mean sea level. With a difference of 60 $nm\,s^{-2}$ between the gravimetric observations on the upper land (ZLS and CG6) and lower land (CG5) of Heligoland, the varying impact of the height-dependent signals from the local sea level shows up significantly. These figures confirm the results of Fratepietro *et al.* (2006) estimating 60–80 $nm\,s^{-2}$ and −20 to −30 mm, respectively, during a storm surge of 2 m sea level increase on the northwest European shelf. Goto *et al.* (2021) report significant sub-$nm\,s^{-2}$ OTL differences from a gravity gradiometer setup based on three closely positioned iGrav superconducting gravimeters (SGs) caused by varying height-dependent effects on those gravimeter sites with distances between 80 and 94 m from the coast. They confirm these findings with ocean tide model values using the software package GOTIC2 (Matsumoto *et al.* 2001) including high accurate land-sea boundaries. Kennedy *et al.* (2014) and Carrière *et al.* (2021) use laterally and vertically, respectively, spaced gravity gradiometer setups based on two SGs for an improved analysis of local hydrological mass variations with an enhanced sensitivity towards local signals between the gravimeters and to eliminate large-scale signals commonly observed by both gravimeters.

Several studies focus on the comparison of global ocean tide models on the basis of terrestrial gravimetry (stationary sensors) with analysed OTL signals. Boy *et al.* (2003) as well as Baker & Bos (2003) use data from worldwide distributed SGs from the Global Geodynamics Project (GGP; Crossley *et al.* 1999) which has been transferred into the IAG Service International Geodynamics and Earth Tide Service (IGETS; Boy *et al.* 2020). Boy *et al.* (2003) find differences of a few $nm\,s^{-2}$ between OTL amplitudes from various global ocean tide models and software packages as well as from SG time-series which are significantly larger than the uncertainty estimates from the SG time-series of a few 0.01 $nm\,s^{-2}$. Lysaker *et al.* (2008) use FG5 absolute gravity measurements for the investigation of ocean tide models on near-coastal stations in Norway at the 10 $nm\,s^{-2}$ level including the modelling of the direct Newtonian attraction by local tide gauge observations. LaCoste & Romberg spring gravimeter observations with electrostatic feedback are used by Bos *et al.* (2002) at Ny Alesund, Spitsbergen, and Neumeyer *et al.* (2005) near Santiago de Cuba with differences at the level of 10 $nm\,s^{-2}$ between OTL amplitudes from global ocean tide models and gravimetric observations. These discrepancies are much larger than the differences of a few $nm\,s^{-2}$ between the various ocean tide models. Clear improvements are found by including local tide gauge observations and a clear statement is provided that high-accuracy gravity measurements (e.g. with SGs), especially for stations near the coastal lines, should take into account tide gauge measurements for the ocean loading correction.

Several publications deal with the comparison of ocean tide models based on vertical displacements from continuous GPS observations on inland and coastal stations. Yuan & Chao (2012) as well as Yuan *et al.* (2013) analyse the OTL vertical displacements for the eight major diurnal and semidiurnal tidal waves from a Western United States and from a global GPS network, respectively, with RMS misfits between GPS observations and global ocean tide models of 0.1 (Q_1, N_2) to 1.8 mm (K_1) with GPS uncertainty estimates (RMSE from least-squares adjustment) of 0.3 mm for Q_1, O_1, N_2
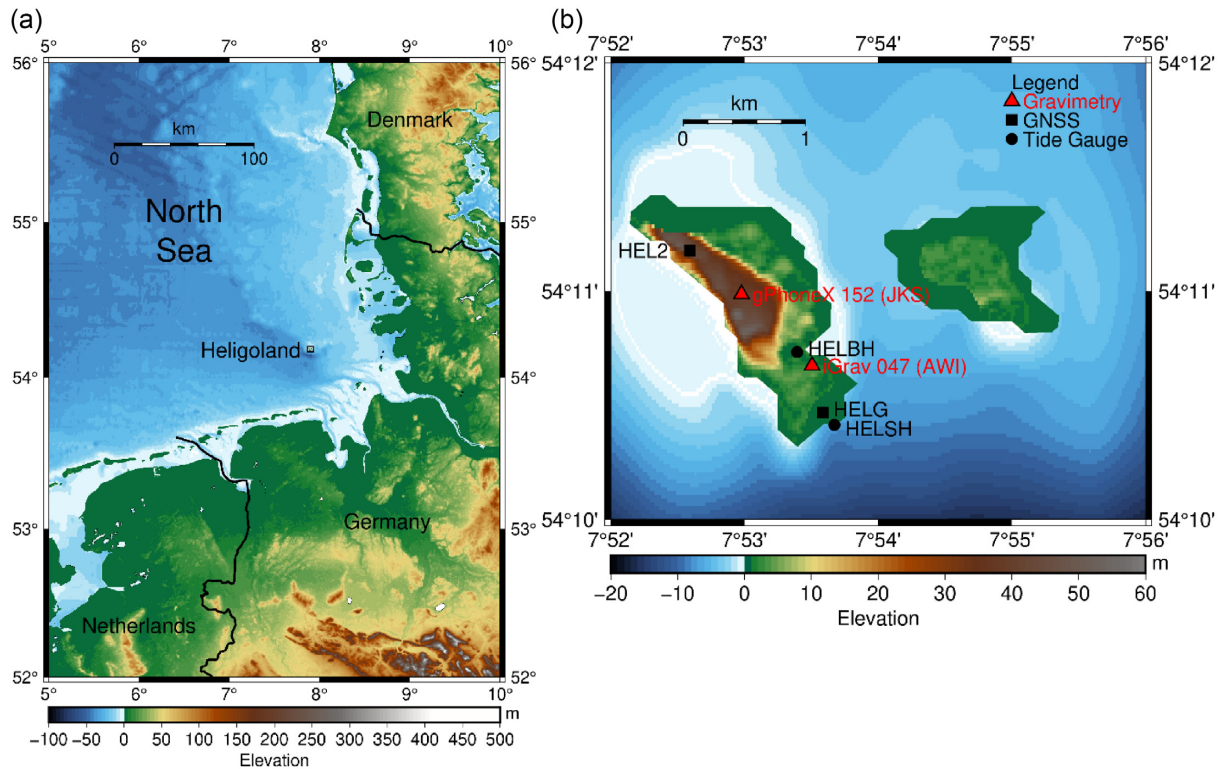
Figure 1. Bathymetry and topography around the island of Heligoland located in the German Bight of the North Sea (a), a zoom to the island of Heligoland with the analysed sensor names (b). Please note the different scaling of the elevation.

and M_2, 1.2 mm for P_1 and S_2, and 2.2 mm for K_2 and K_1. Penna *et al.* (2015) analyse OTL displacements in Western Europe and estimate horizontal as well as vertical displacement uncertainties with 0.2 mm from at least 4 yr of observations and process noise optimization.

This study covers the estimation of OTL parameters based on two continuous gravimetric time-series from the SG iGrav 047 on the lower land and from the spring gravimeter gPhoneX 152 on the upper land of the island of Heligoland. Due to the small distances between the gravimeter sites and to the shoreline, the gravimetric signals contain significant contributions from the Newtonian attraction by sea mass variations in the direct vicinity (within a region of 10 times the instrument height). These contributions are proportional to the local sea level only (like a tide gauge), strongly height-dependent and thus different for both gravimeter sites. For the reduction of these entirely local tidal and non-tidal signals from the gravimetric observations at both sites, a method based on local tide gauge observations and empirical transfer functions is introduced that does not require precise knowledge of the coastline. The remaining height-independent OTL parameters from both gravimetric time-series are expected to match within their instrumental uncertainties to prove the efficiency of this method. The height-independent OTL gravity parameters reflect regional OTL signals with the large-scale vertical displacement as a dominating contributor to the gravimeter measurements. This justifies an approximate, but nevertheless high-accuracy, transition to OTL vertical displacements, which is fully independent of any GNSS data and processing and presented as by-product of this study for near-coastal sites. In this way, this study presents the essential prerequisites for the analysis of regionally representative height-independent non-tidal ocean loading signals in the North Sea, which will be investigated in future studies.

Recent ocean tide models, for example FES2014b (Lyard *et al.* 2021), EOT20 (Hart-Davis *et al.* 2021), TPXO9.5a (Egbert & Erofeeva 2002), GOT4.10c (Ray 2013) and HAMTIDE (Taguchi *et al.* 2014), provide OTL parameters with differences of up to a few $\mathrm{nm\,s^{-2}}$ and a few mm in gravity and vertical displacements, respectively, for coastal sites (Penna *et al.* 2008). Larger deviations between OTL modelling and gravimetric observations may indicate systematic errors in the ocean tide model, the OTL computation and/or the observations. At the island of Heligoland, the differences between the OTL parameters from the ocean tide models are up to $2\,\mathrm{nm\,s^{-2}}$ and 1 mm, respectively, for the eight major diurnal and semidiurnal waves. SG observations are expected to provide OTL gravity signals with uncertainties at the $0.1\,\mathrm{nm\,s^{-2}}$ level and better depending on the length of the time-series, while GPS/GNSS observations should yield a precision of 0.2 mm (Penna *et al.* 2015). Based on these figures, this study aims primarily at providing the best estimates of OTL parameters in terms of height-independent gravity for the island of Heligoland at an uncertainty level of a few $0.1\,\mathrm{nm\,s^{-2}}$. As by-product, OTL vertical displacements are provided at an uncertainty level of a few 0.1 mm also from the SG observations.

2 OBSERVATIONS

A redundant set of geodetic and oceanographic sensors is available on the island of Heligoland (Fig. 1b, Table 1) as well as other geophysical data sets e.g. from a permanent network of broad-band seismometers (Becker *et al.* 2020). During winter 2018–2019, the sensor network had been enhanced by three spring gravimeters (Weise *et al.* 2020). Another spring gravimeter Scintrex CG6-171 has been observing from Oct 2019 to May 2020 to record non-tidal

Table 1. Basic information on existing sensors and analysed periods on the island of Heligoland. For the transition to normal heights referring to the German height reference system DHHN2016, a height anomaly of 39.16 m must be subtracted from the given ellipsoidal heights.

Sensor type	Sensor name	ETRS89 coordinates (lat, lon, h)	Period
Gravimeter	iGrav 047 (AWI)	54.17790°, 7.89176°, 41.47 m	2020–03-13–2022–03-01
Gravimeter	gPhoneX 152 (JKS)	54.18312°, 7.88297°, 80.51 m	2020–02-25–2021–06-23
Tide Gauge	HELBH	54.1789°, 7.8900°, 34.14 m	2000–01-01–2022–03-01
Tide Gauge	HELSH	54.1750°, 7.8943°, 34.15 m	2000–01-01–2022–01-01
GNSS	HELG	54.1745°, 7.8931°, 48.38 m	2017–01-01–2021–10-31
GNSS	HEL2	54.1863°, 7.8765°, 92.20 m	2017–01-01–2021–10-31

ocean loading during another winter period. The continuously operating gravimeters iGrav 047 and gPhoneX 152 used in this study have been installed in parallel in Feb-Mar 2020. The iGrav 047 has been in nominal operation since 13 March 2020 after cooling down to 4 K including vacuum pumping. The Helgoland Gravimetric Observatory Germany (HELGOG) is installed in the basement of the Biologische Anstalt Helgoland (BAH) of Alfred-Wegener-Institute (AWI) with an iGrav 047 sensor height of $H_0 = 2.31$ m above mean sea level and a distance of approximately 15 m from the sea with the shoreline being variable with sea surface heights. HELGOG participates in IGETS by providing level 1 raw gravity and atmospheric pressure data (sensor 'he047') with sampling rates of 1 s and 1 min (Voigt *et al.* 2020) on a regular basis to the publicly accessible IGETS database hosted by GFZ (Voigt *et al.* 2016b).

The pre-processing of raw gravity observations in 1 s sampling follows exactly the procedure from Voigt *et al.* (2021). The time-series showed three steps, on 3 June 2020 during the drilling of holes in the floor, on 30 June 2021 after replacing the GPS antenna and cable, and on 2 December 2021 due to an error of the uninterruptible power supply and reboot of the NUC (Next Unit of Computing) PC. Two absolute gravimetric measurements from 2 to 5 July 2020 and 22 to 25 June 2021 at HELGOG are used for the estimation of the iGrav 047 amplitude factor with -943.427 nm s^{-2} V^{-1} and a RMSE of 1.203 nm s^{-2} V^{-1} (relative uncertainty of 1×10^{-3}) and the linear drift of $+46.0$ nm s^{-2} yr^{-1}. Both absolute gravimetric time-series provide the same mean gravity value of $g = 9.814\ 054\ 337$ m s^{-2}, which can be found in the Absolute Gravity Database (AGrav; uploaded by Timmen) hosted by the International Gravimetric Bureau (BGI) and BKG (Wilmes *et al.* 2009). As the AGrav database is currently not online, the documentation of the absolute gravity determinations in 2020 and 2021 at Heligoland are also available from the Institutional Repository of Leibniz Universität Hannover (Timmen 2020, 2021). As explained in Timmen *et al.* (2021), an instrumental uncertainty of 20 nm s^{-2} can be stated for a g-determination (mean *g*-value from a few days of measurements) with the Hannover FG5 gravimeter. This empirical estimate is based on the results obtained by participating in international metrological comparisons of absolute gravimeters.

For the realization of a gravity gradiometer, gPhoneX 152 was installed in Feb 2020 and observed until June 2021 over 1.5 yr in the seismic station Heligoland in the basement of James–Krüss–Schule (JKS). JKS is located on the upper land at an elevation of $H_0 = 41.35$ m above mean sea level at a horizontal distance of 800 m from iGrav 047 at AWI and an approximate distance from the coast of 230 m. The seismic station is operated by the Institute of Geosciences, Christian–Albrechts–Universität zu Kiel. The calibration of the gPhoneX 152 was verified by comparing analysed tidal amplitudes (tidal groups O$_1$, P$_1$, K$_1$, M$_2$) with results from three well-calibrated gravimeters with registrations at the same site: ZLS Burris B64 (2018-08-30–2019-06-28), Scintrex CG6-49

(2018-11-18–2019-04-04), Scintrex CG6-171 (2019-10-17–2020-06-04). All three gravimeters were calibrated in the Gravity Meter Calibration System Hannover (Timmen *et al.* 2020) before and after their deployment on Heligoland. The uncertainty of the gPhoneX 152 calibration factor may be estimated to a few parts in 1000. The irregular drift is estimated separately for two periods. For the initial period until 27 June 2020 (first 4 months of observations), the drift is modelled by a logarithmic function while the second period is modelled by a quadratic polynomial. A gap from 27 June to 6 July 2020 appears after a Windows update and is filled with iGrav 047 data for spectral analysis. The raw gravity and atmospheric pressure data with sampling rates of 1 s and 1 min of the gPhoneX 152 at Heligoland used in this study are also available from the IGETS database (sensor 'he152').

In addition, there are two long-term tide gauge stations. HELBH is located in the more quiet inland harbour and only 200 m from the iGrav 047 SG site at AWI and thus well-suited for representing the local sea level next to the gravimeter. HELSH is located at the south harbour and known to be disturbed by frequent wind driven effects. This is why solely HELBH is used for tidal analysis in this study, 22 yr of observations in total. Both tide gauges are operated by WSV (Federal Waterways and Shipping Administration). Current data from the past 30 d are available in daily files from WSV (2022), while long time-series are available upon request from BfG (2022).

Finally, there are two continuously operating GNSS stations. HELG is part of the EUREF permanent GNSS network station and the antenna was installed in 1999 on top of a steel mast anchored to a wall of the building of the waterways and shipping office in the south harbour on the lower land at an elevation of 9 m above mean sea level. HEL2 is part of the GREF (Geodetic Reference Frame of Germany) and the antenna was installed on top of a concrete pillar in 2005 on the upper land at an elevation of 53 m above mean sea level. Both GNSS stations were installed and are frequently maintained by BKG (German Federal Agency for Cartography and Geodesy). Raw data are available from BKG (2022), while the processed data are provided by Deng (2023). Almost 5 yr of GNSS observations are processed using the Precise-Point-Positioning (PPP) method. The satellite orbit and clock products from the second GFZ reprocessing and routine product are fixed (Deng *et al.* 2015; Rebischung *et al.* 2016). The daily PPP coordinate solution has an uncertainty of 2 and 4 mm in the horizontal and vertical component, respectively. To estimate coordinates in a time sampling of 1 hr, the random-walk constrain is applied on 30 hr observations. The central 24-hr coordinates are the final solution to reduce the day boundary jumps from the orbit and clock products. While a 30-hr orbit is fixed on the second GFZ reprocessing and routine product, the satellite clock biases are calculated using up to 140 global IGS stations. Based on the 30-hr orbit and clock products, the PPP coordinates with a time sampling of 1 hr are estimated. This solution is specifically designed for the analysis of non-tidal ocean loading signals, especially storm

surges of a few hours, and contains residual day boundary jumps up to 10 mm in the coordinate time-series. For the tidal analyses of this study, the model-based OTL corrections, originally reduced from the observations, are restored.

3 METHODS

3.1 Ocean tide loading

Gravimetric time-series observed with gravimeters at the surface of the Earth include OTL effects as the combination of the direct Newtonian attraction, the vertical displacement in the undeformed gravity field of the Earth associated to the load Love number *h'*, and the change in the gravity potential due to mass redistributions induced by the elastic deformation associated with load Love number *k'*. The direct Newtonian attraction consists of a large local and a small non-local effect (Jentzsch 1997; Agnew 2007; Torge & Müller 2012). As the local Newtonian attraction effect cannot be captured with spherical harmonic decomposition (Merriam 1980), the OTL effects are usually computed with Green's functions on the basis of ocean tide models (Farrell 1972). Models under investigation are FES2014b, EOT20, TPXO9.5a, GOT4.10c and HAMTIDE. Within this study, the model-based OTL parameters are computed from the OTL provider (Bos & Scherneck 2022) and used for numerical analyses in Section 4, as this is the standard tool commonly used in terrestrial gravimetry. In addition, tidal parameters are well observable with continuously operating gravimeters, but these empirical parameters represent the combined effects of solid Earth and ocean tides. For separating the OTL parameters, the reduction of an Earth body model is required according to Jentzsch (1997) or Ducarme & Kääriäinen (1980) including RMSE propagation. For this purpose, an ellipsoidal Earth model with an inelastic mantle and a non-hydrostatic initial state (DDW-NHi; Dehant *et al.* 1999) is used. The initially local phases from the analyses of the gravimetric and GNSS time-series are converted into phases relative to Greenwich according to Boy *et al.* (2003) for the comparison with the results from the OTL provider. The OTL parameters are denoted as *L* (OTL amplitudes) and λ (OTL phases relative to Greenwich).

3.2 Tidal analysis of the geodetic and oceanographic time-series

For the tidal analysis of the gravimetric time-series from iGrav 047 and gPhoneX 152, the GNSS time-series HELG and HEL2 as well as the HELBH tide gauge time-series, all in 1 hr time sampling, the ET34-X-V80 software (Schueller 2015, 2020) is applied along with the tide generating potential catalogue by Hartmann & Wenzel (1995). The wave grouping is done according to the standards recommended by Ducarme & Schueller (2019) for time-series of 0.75–2 yr of observation. The main results are the estimated tidal parameters (amplitudes and local phases from the combined effects induced by solid Earth and ocean tides) in the gravimetric and GNSS time-series with given local phase leads being positive (lags negative) for the linear tides, while the phase estimates for the non-linear tides are relative to Greenwich (Schueller 2020, Users Guide, p. 111). The tidal analysis of the tide gauge time-series directly provides ocean tide parameters (amplitudes and phases) with phases relative to Greenwich and phase lags being positive (leads negative) as defined in the conventions of oceanography (Schueller 2020, Users Guide, p. 52).

The tidal analyses are computed consistently with the same input parameters for every time-series. After high-pass filtering of the time-series, 30 diurnal, 28 semidiurnal and 7 ter-diurnal waves according to standard wave grouping (Ducarme & Schueller 2019) are estimated as well as 9 diurnal, semidiurnal and ter-diurnal degree-3-waves (3 each) and additional non-linear waves (from diurnal to 1/12-diurnal) including M_6, M_8, M_{10} and M_{12}, which are not part of the tide generating potential catalogue by Hartmann & Wenzel (1995). Along with the tidal waves, the single admittance factors between gravity and barometric pressure are determined for both gravimetric time-series. Fig. 2 shows the power spectral densities (PSD) of the gravity residuals from iGrav 047 (AWI) and gPhoneX 152 (JKS) after tidal analysis with ET34-X-V80 (i.e. channel 1 of res-file; Schueller 2020, Users Guide, p. 244). The one-sided PSD are estimated according to Welch (1967). The time-series are divided into the longest possible segments to obtain as close to but not exceed eight segments with 50 per cent overlapping, applying a Hamming window function to each segment. A strong signal reduction is visible in the diurnal and semidiurnal band for the height-independent component of both iGrav 047 (AWI) and gPhoneX 152 (JKS) compared to the total gravity signal (see following section). In the higher frequency band (4 cpd and higher), significant peaks are still visible, as the empirical reduction method presented in the following section uses up to quadratic but no cubic transfer functions.

3.3 Empirical reduction of local Newtonian attraction from gravimetric observations

The aim of this study is the extraction of OTL signatures in the North Sea from gravimetric time-series. The approach presented here is based on the decomposition of the total gravity signal g_{tot} into a height-independent (Δg_{hi}) and a height-dependent (Δg_{hd}) component by $g_{tot} = \Delta g_{hi} + \Delta g_{hd}$ (Fig. 3), which are introduced in the following.

3.3.1 Height-independent gravity component

Although tide gauge measurements provide information about the sea level at a single point, denoted $\zeta_0 = \zeta(\mathbf{x}_0)$, gravimetric measurements integrate information about the global ocean load function, denoted $\rho_{sw} \zeta(\mathbf{x})$, where ρ_{sw} is the seawater density and $\zeta(\mathbf{x})$ the global sea level function. The integral signal can be described by the convolution of the global ocean load with the Green's function for gravity $G_{tot}(H_0, |\mathbf{x} - \mathbf{x}_0|)$ (e.g. Farrell 1972; Agnew 2013), or by expanding the ocean load into a series of spherical harmonic functions. The Green's function for gravity comprises a large-scale component representing the effect of the solid Earth response to loading and the Newtonian attraction of distant mass anomalies and a small-scale component induced by the Newtonian attraction of mass anomalies in the direct vicinity of the gravimeter. The large-scale component can be isolated by assuming the effect of point mass loading at geoid level (i.e. undisturbed sea surface) on an integration point at geoid height. The resulting integral is height-independent and can be written as

$$\Delta g_{hi}(\zeta(\mathbf{x})) = \rho_{sw} \int_O dA\, G_{tot}(H_0 = 0, |\mathbf{x} - \mathbf{x}_0|)\, \zeta(\mathbf{x}). \qquad (1)$$

Here, the integration is performed over the entire ocean, denoted *O*. The height-independent gravity component is dominated by long wavelengths, and thus only weakly varies in horizontal direction.
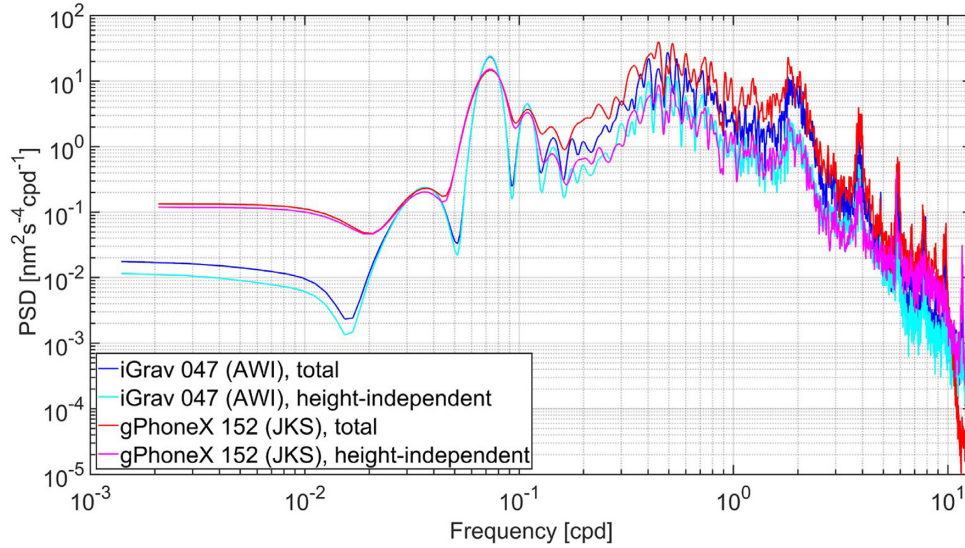
Figure 2. Power spectral densities (PSD) of the total and height-independent gravity residuals from iGrav 047 (AWI) and gPhoneX 152 (JKS) after tidal analysis.
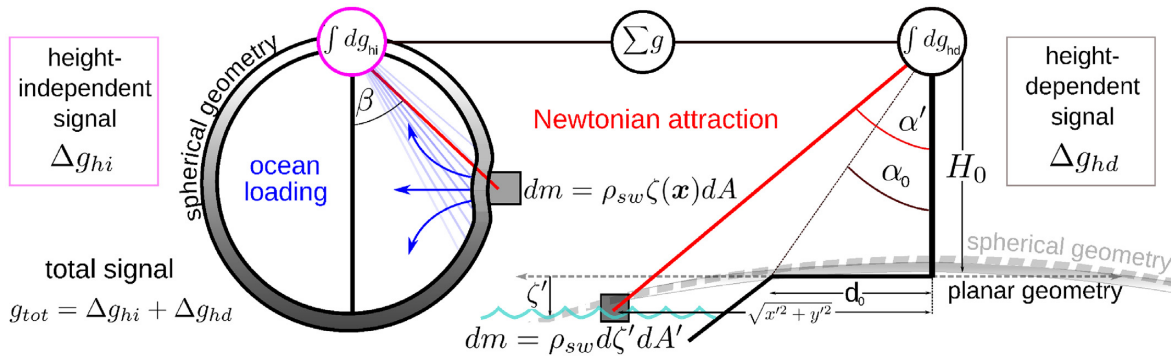

Figure 3. Definition of the height-independent versus the height-dependent gravity component that add up to the total gravity signal, that is $g_{tot} = \Delta g_{hi} + \Delta g_{hd}$. While Δg_{hi} is defined by an integral of point loads over the whole sphere, Δg_{hd} is obtained by conducting a planar integral under consideration of Newtonian attraction by vertically extended mass elements.

The evaluation at sea level effectively suppresses the local Newtonian attraction in the direct vicinity of the evaluation point $\mathbf{x}_0$. Still, Newtonian attraction is exerted by distant mass elements, but the height-independent component is largely dominated by solid Earth deformation. In summary, the height-independent gravity component is non-local and linear in ζ and requires integration over the entire globe (Fig. 3, left-hand side).

3.3.2 Height-dependent gravity component

Gravity recordings at any altitude different from zero are, however, significantly affected by the Newtonian attraction of oceanic mass anomalies nearby. We call this effect 'height-dependent gravity contribution', which can be recovered by evaluating

$$\Delta g_{hd}(H_0, \zeta_0) = \rho_{sw} \int_O dA \, \delta G(H_0, |\mathbf{x} - \mathbf{x}_0|) \zeta(\mathbf{x})$$

$$\cong G\rho_{sw} \int_0^{\zeta_0} d\zeta' \int_{O(\zeta')} dA' \frac{H_0 - \zeta'}{\left((H_0 - \zeta')^2 + \delta'^2\right)^{3/2}}. \quad (2)$$

Here, the convolution with the difference Green's function $\delta G(H_0, |\mathbf{x} - \mathbf{x}_0|) = G_{tot}(H_0, |\mathbf{x} - \mathbf{x}_0|) - G_{tot}(0, |\mathbf{x} - \mathbf{x}_0|)$ is shifted to planar geometry in cylindrical coordinates, with ζ' and $\delta' =$

$\sqrt{x'^2 + y'^2}$ as variables of vertical and horizontal integration, respectively. Significant weights are only assigned to mass elements with lateral distances up to $\delta' = 10H_0$, where the Earth's curvature is negligibly small. Further, the sea level function is assumed to be dominated by wavelengths longer than $10H_0$, and thus approximated to be constant, equal to ζ_0. The integration is performed over all wet grid cells at a certain sea level, denoted $O(\zeta')$. The weak height dependence of gravity induced by solid Earth deformations is neglected (*cf.* e.g. Olsson *et al.* 2009). In addition, the transition to the planar approximation induces a minor deviation. However, both effects are negligibly small for the presented approach. In summary, the height-dependent gravity component strongly depends on the horizontal position and the height of the integration point. The influence by the local sea level can be obtained by solving a planar integral in the direct vicinity of the gravimeter (Fig. 3, right-hand side). In addition, it can be potentially non-linear in the local sea level, depending on the exact placement of the gravimeter with respect to the coastline. This field component can be seen to behave like a tide gauge measurement, with a complex, non-linear and a priori unknown dependency on the local sea level ζ_0. While the height-independent component contains signatures of large-scale ocean loading, the 'tide-gauge-like' height-dependent effect
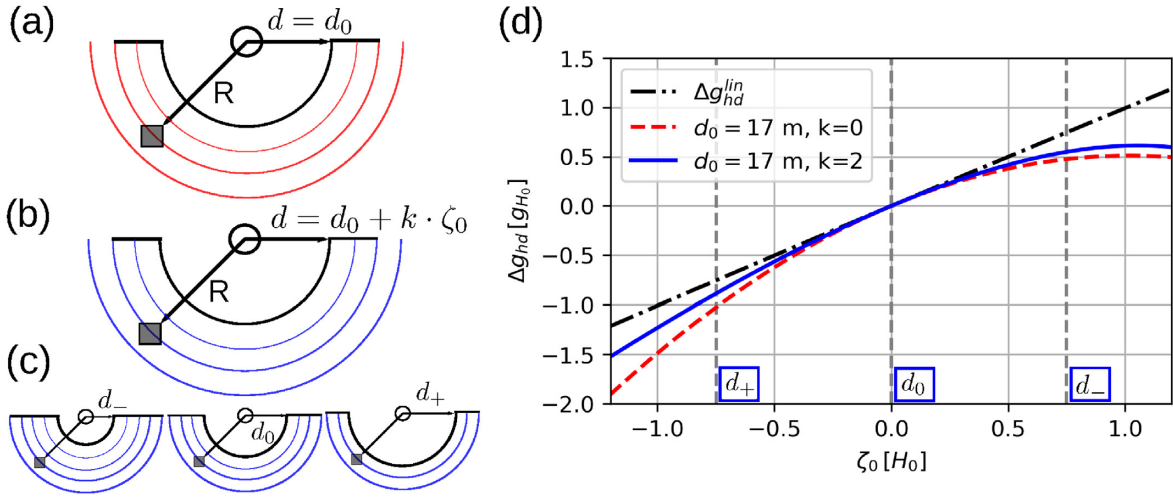
Figure 4. Characteristics of the height-dependent gravity component for a simplified semicircular model. The model is evaluated for (a) a constant radius d_0 (red) and (b, c) with drying/wetting, that is $d = d_0 + k\zeta'$ (blue). The respective gauge functions (d) show a clear deviation from the linear approximation (black, dashed dotted), while $k > 0$ (blue) reduces the quadratic non-linearity with respect to $k = 0$ (red). Parameters are chosen to represent the environment of the AWI site.
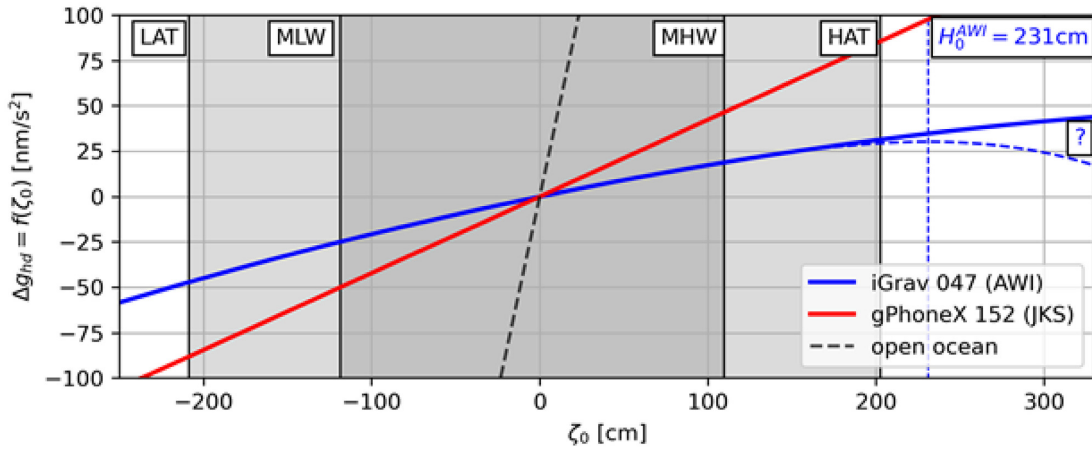

Figure 5. Transfer functions $\Delta g_{hd} = f(\zeta_0)$ as estimated for AWI (blue) and JKS (red) and the maximum possible effect if the gravimeter was placed over the open ocean (black, dashed). Overlain a number of tidal levels, including MHW/MLW (mean high/low water), and HAT/LAT (highest/lowest astronomical tide), are presented spanning the range of validity for the transfer functions. When extrapolating beyond HAT, the validity of the transfer function is questionable, especially for site AWI, where the slope of the function changes sign at $H_0 = 231$ cm, indicated by a proposed cubic extension applied for $\zeta_0 > $ MHW (blue dashed).

superimposes these signatures and must be removed in order to assess the desired information. Before discussing how the height-dependent component can be reduced from gravimeter measurements, the origins of its potential non-linearity are discussed.

3.3.3 Non-linearity of the height-dependent component

For $\zeta' > H_0$, the integrand of eq. (2) changes its sign. This points to the fact that non-linearity is expected if ζ_0 is a significant fraction of H_0, because in this case the angle α', that mass elements enclose with the vertical, changes significantly with ζ'. In contrast, the corresponding angle for the height-independent effect β remains by definition independent of H_0 and ζ' (Fig. 3). The integral (eq. 2) is expanded into a first-order Taylor expansion in ζ' and the resulting expression is solved analytically for a gravimeter positioned on a semicircular peninsula with radius d_0 at height H_0 (Figs 4a and 3).

The dimensionless expression

$$\frac{\Delta g_{hd}(H_0, \zeta_0)}{g_{H_0}} = \frac{\zeta_0}{H_0}\left(1 - \frac{1}{2}(\sin\alpha_0)^2 \frac{\zeta_0}{H_0}\right) \quad (3)$$

is obtained suggesting the linear relation $\Delta g_{hd}^{lin} = g_{H_0}\frac{\zeta_0}{H_0}$ for $\zeta_0 \ll H_0$. The constant of proportionality is $\frac{g_{H_0}}{H_0} = \pi G \rho_{sw} \cos\alpha_0$ with $\tan\alpha_0 = d_0/H_0$ (Fig. 4b). It is proportional to $\cos\alpha_0 = \frac{H_0}{\sqrt{d_0^2 + H_0^2}}$, which means that its maximum is obtained for $d_0 = 0$. Recalling that d_0 is the horizontal distance between gravimeter and coast and H_0 is the height of the gravimeter, this would position the gravimeter directly over the shoreline and corresponds to half the value obtained over the open ocean: $2\pi G \rho_{sw} = 429.4 \frac{nm}{s^2 m}$ (Fig. 5). Fig. 4(d) shows the relation displayed in eq. (3), indicating a significant quadratic (non-linear) behaviour when $|\zeta_0|/H_0$ approaches 1. In addition, the coastline might change with the instantaneous sea level, if the coastal margins are not vertical walls, but gently sloping beaches. This causes drying and wetting of coastal areas

and a change of the area of integration. Integral (eq. 2) is solved numerically while assuming $d = d_0 + k\zeta'$ as variable coastline. The iGrav 047 site at AWI is represented by an undisturbed distance of $d_0 = 17$ m between gravimeter and coast and a gravimeter height of $H_0 = 2.31$ m. Interestingly, the effect of drying and wetting counteracts the quadratic non-linearity for $k > 0$, which is typical for most coasts (Figs 4b–d). While this simplified model succeeds in explaining the origin and functionality of the effects in general, the realistic coastal situation is too complex to be captured by this approach. Numerically solving eq. (2) under consideration of high-resolution bathymetric and coastline data is one way to model the height-dependent effect. On the other hand, these data sets are not available for arbitrary observation sites and are potentially hard to recover in sufficiently high detail. Therefore, an empirical approach is presented here that relies on the similarity of the height-dependent 'tide gauge-like' effect to the local sea level (as sampled by a tide gauge).

3.3.4 Empirical modelling approach for the height-dependent component

The prior discussion motivates that (a) a height-dependent gravity component is to be expected on a scale of $\pi G \rho_{sw} \cos \alpha_0 \zeta_0$, that is scaling with $\cos \alpha_0$, and that (b) non-linearities become relevant if $\frac{|\zeta_0|}{H_0} \approx 1$. For the JKS site, only (a) is fulfilled with $(\cos \alpha_0, |\zeta_0|/H_0) \approx (0.19, 0.05)$ while both conditions are fulfilled at AWI $(0.12, 0.7)$. Additionally, it is known that the shoreline varies with ζ_0 in the direct vicinity of both gravimeters. Our aim is thus to find the general non-linear function

$$\Delta g_{hd} = f(\zeta_0) = \sum_{i=1}^{r} f_i (\zeta_0)^i = f_1 \zeta_0 + f_2 \zeta_0^2 + f_3 \zeta_0^3 + \dots \quad (4)$$

for both gravimeters. Formally, this function can be recovered from the relation $\Delta g_{hd} = g_{tot}(t_i) - \Delta g_{hi}(\zeta(\mathbf{x}, t_i))$, where $\zeta(\mathbf{x}, t_i)$ is the time-series of the global sea level function, and $g_{tot}(t_i)$ are the gravimeter measurements. This is in contrast to our goal of obtaining information about $\zeta(\mathbf{x}, t_i)$ by using gravimetric loading signals. Further, it is not feasible, because $\zeta(\mathbf{x}, t_i)$ is not accurately known at arbitrary epochs t_i. This is different when considering ocean tide signals that are responsible for the largest part of the sea surface variability. For a tidal constituent labelled j, the global sea level function $\zeta^j(\mathbf{x})e^{i\omega_j t}$, and thus the solution of integral (1), $\Delta g_{hi}^j e^{i\omega_j t}$, is accurately known from modern ocean tide atlases. The FES2014b tidal atlas (Lyard *et al.* 2021) is used in combination with the program NLOADF (Agnew 2013) and the Gutenberg–Bullen Earth model from software package SPOTL (setting $H_0 = 0$ in agreement with (1) for calculation of $\Delta g_{hi}^j \in \mathbf{C}$ from the global tidal sea surface mass anomaly $\zeta^j(\mathbf{x}) \in \mathbf{C}$). Here the real and imaginary parts refer to in-phase and quadrature components of the tidal oscillation, respectively. The tidal constituents g_{tot}^j are estimated for the gravimetric time-series and the tide gauge time-series with ET34-X-V80 as described in Section 3.1. Together, the reduced gravity time-series

$$\Delta g_{hd}^{tid} = \sum_{j=1}^{N} Re\left(\left(g_{tot}^j - \Delta g_{hi}^j\right) e^{i\omega_j t}\right) \quad (5)$$

includes only the height-dependent component related to the local sea level $\zeta_0^{tid} = \sum_{j=1}^{M} Re(\zeta_0^j e^{i\omega_j t})$ by

$$\Delta g_{hd}^{tid} = f\left(\zeta_0^{tid}\right). \quad (6)$$

The notation $\Delta g_{hd}^j = (g_{tot}^j - \Delta g_{hi}^j) \in \mathbf{C}$ is introduced. When expanding eq. (6), the non-linearity of eq. (4) induces the interaction of individual partial tides included in ζ_0^{tid}, for example the gravimetric M_4-tide is induced via f_1 by the local M_4 sea surface tide ($\omega_{M_4} = \omega_{M_4}$), but also via f_2 by interaction of M_2 with itself ($\omega_{M_4} = \omega_{M_2} + \omega_{M_2}$) and many other combinations. Comparing the coefficients with the same temporal harmonic behaviour $\sim e^{i\omega t}$ on both sides of eq. (6), the system of N linear equations

$$\delta(\mathbf{f_r}) = \mathbf{I}_{N \times r} \cdot \mathbf{f}_r^T - \left(\Delta g_{hd}^1, \Delta g_{hd}^2, \dots, \Delta g_{hd}^N\right) = 0 \quad (7)$$

is extracted considering N gravimetric partial tides, M partial tides of the local sea surface elevation and the general non-linear function $f(\zeta_0)$ up to order r. Matrix $\mathbf{I}_{N \times r}$ describes all possible interactions that induce gravimetric variations at the frequency of a certain partial tide and $\mathbf{f}_r = (f_1, f_2, \dots, f_r)$. $N > r$ is selected to overdetermine eq. (7). The individual components of the transfer function $f(\zeta_0)$ can now be obtained by minimizing the RMSE of $\delta(\mathbf{f}_r)$, that is RMSE $= \sqrt{\sum |\delta_j|^2}$ under variations of $\mathbf{f}_r$, with the constraint $f_i \in \mathbf{R}$, as the local Newtonian attraction is in-phase with the local sea surface variations.

### 3.3.5 Empirical transfer functions for sites JKS and AWI

Before conducting the described minimization procedure, an ensemble of partial tides must be selected. The following conditions are considered: (a) large amplitude in the gravimetric and tide gauge time-series, (b) availability from the FES2014b tidal atlas to allow the subtraction of the height-independent component and (c) inclusion of non-linear, shallow-water tides that are sensitive to f_2. Based on these criteria, it is decided to concentrate on semidiurnal tides as they are resonant in the German Bight, and leave out long-period and diurnal tides due to their rather small amplitudes. The partial waves M_2, N_2, μ_2, K_2 and S_2 are included. Additionally, the shallow-water tides M_4, MS_4 and MN_4 are included for effective estimation of f_2. Minimization of the RMSE is performed for the described $N = 8$ partial tides in the gravimetric time-series and $M = 128$ partial tides of the local sea surface elevation with periods ranging from 1 yr to 12 cycles per day. Transfer functions up to $r = 3$ for both gravimeters are fitted (Table 2). It is evident that the RMSE won't rise when allowing for additional degrees of freedom of $f(\zeta_0)$. While the improvement at the JKS site is quite small for $r > 1$, the RMSE for AWI decreases by 17 per cent for $r = 2$. Based on these findings, $r = 1$ for JKS and $r = 2$ for AWI are selected with the functions displayed in Fig. 5 together with tidal levels constructed from $M = 128$ partial tides. The derived transfer functions are optimized based on the tidal sea surface variability spanned by LAT to HAT (lowest and highest astronomical tide, respectively). It should be noted that the transfer function for the iGrav 047 at AWI cannot be expected to be accurate for $\zeta_0 > $ HAT, as in fact (2) indicates that $\frac{df}{d\zeta_0}(H_0) = 0$, which is not true for the derived function (Fig. 5). For the analysis of extreme events, for example large storm surges, a proper extension for $\zeta_0 > $ MHW (mean high water) should be constructed, for example under inclusion of cubic or higher-order dependencies.

3.3.6 Phasor plots for tidal gravity field components

The effect of the transfer functions can also be visualized with phasor plots of the tidal constituents presented in Fig. 6. Several features can be identified. First, the phases of the

Table 2. Empirical transfer functions of orders $r = 1, 2, 3$ for the iGrav 047 at AWI and for the gPhoneX 152 at JKS from tide gauge time-series HELBH [m] with corresponding RMSE fits. The transfer functions selected within this study are presented in bold font.

Order	Transfer function $f(H_0, \zeta_0)$ [nm s^{-2}]		RMSE [nm s^{-2}]	
r	iGrav 047 (AWI)	gPhoneX 152 (JKS)	AWI	JKS
1	$19.152 \frac{\zeta_0}{\text{m}}$	$\mathbf{42.252 \frac{\zeta_0}{\text{m}}}$	0.801	**1.517**
2	$\mathbf{19.018 \frac{\zeta_0}{\text{m}} - 1.739 \frac{\zeta_0^2}{\text{m}^2}}$	$42.307 \frac{\zeta_0}{\text{m}} + 0.703 \frac{\zeta_0^2}{\text{m}^2}$	**0.668**	1.507
3	$18.200 \frac{\zeta_0}{\text{m}} - 1.661 \frac{\zeta_0^2}{\text{m}^2} - 0.670 \frac{\zeta_0^3}{\text{m}^3}$	$46.798 \frac{\zeta_0}{\text{m}} + 0.274 \frac{\zeta_0^2}{\text{m}^2} - 3.681 \frac{\zeta_0^3}{\text{m}^3}$	0.662	1.425
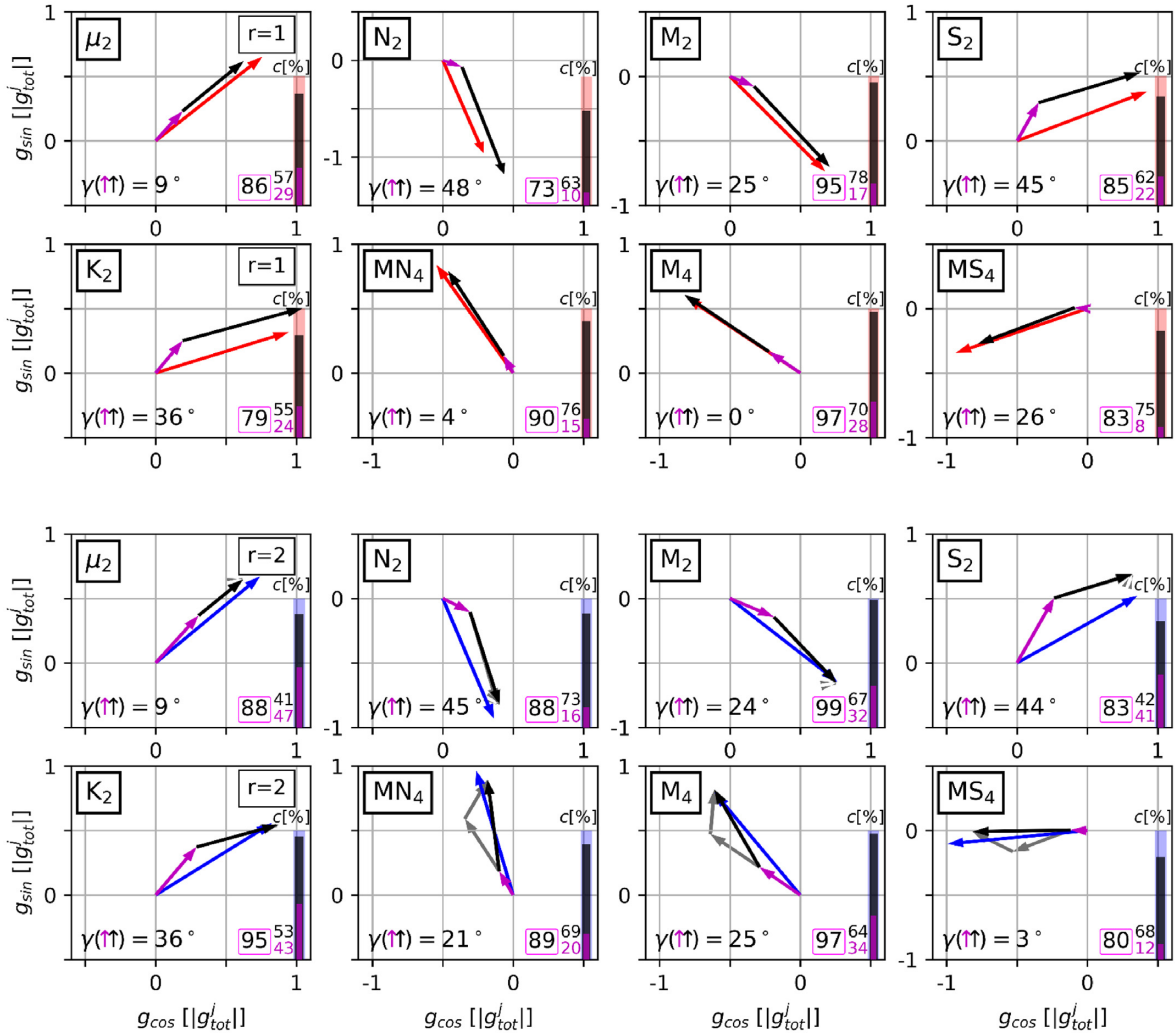
Figure 6. Phasor plots for the selected tidal ensemble evaluated for site JKS (red, $r = 1$) and site AWI (blue, $r = 2$) normalized with the respective total phasor length in Greenwich phase notation. The full gravimetric phasors g_{tot}^j (red/blue) are approximated by combining the height-independent component Δg_{hi}^j (magenta) and the height-dependent component Δg_{hd}^j (black), that differ in direction by angle γ. Additionally, the contributions of orders 1 and 2 are discriminated for $r = 2$ (grey), which clearly improves the captured signal fraction c for the shallow-water tides (M$_4$, MS$_4$, MN$_4$) that is presented as a colour bar (magenta: height-independent component only; black: increase when adding the height-dependent part; magenta box: both effects combined).

gravimetric height-dependent and height-independent components enclose angles $\gamma^j(\Delta g_{hd}^j, \Delta g_{hi}^j)$ up to 48° (for N$_2$). The angles are nearly identical for the semidiurnal tides and for both gravimeters as they are dominated by linear f_1-interaction. Nonetheless, the stronger height-dependent component at JKS causes deviations in the alignment of the total phasors compared to AWI (e.g. for K$_2$). The situation changes for the considered shallow-water tides (MN$_4$, M$_4$ and MS$_4$), where the AWI phasors are strongly influenced by the quadratic f_2–effect, rotating them with respect to JKS

(e.g. M$_4$). This quadratic modification allows close approximation of the whole phasor for these tides and explains the reduction of the RMSE when considering $r = 2$. Also, the captured signal fractions c are calculated for the individual phasors $\mathbf{p}_j$ (the individual gravity components Δg_{hd}^j, Δg_{hi}^j), defined by $c_j = 1 - (|\mathbf{p}_j - g_{tot}^j|)/|g_{tot}^j|$. The comparison of the c_j for the individual partial tides (Fig. 6) confirms that high values from 73 to 99 per cent are only achieved if both gravity components and the non-linearity at site AWI are combined.

3.3.7 Evidence for the importance of a drying/wetting non-linearity at site AWI

By comparison of Figs 5 and 4(d), the non-linear AWI transfer function can partially be attributed to a $k > 0$ drying/wetting effect. In fact, for $k = 0$ the simple model (eq. 3) predicts the ratio

$$\frac{f_2}{f_1} = \frac{-(\sin \alpha_0)^2}{2 \, H_0} = -0.21 \text{ m}^{-1}. \tag{8}$$

Instead, $\frac{f_2}{f_1} = -0.09$ m^{-1} is found pointing to significant contributions by $k > 0$ that tend to attenuate the second order effect (Fig. 3d).

In summary, the empirical transfer functions between the local sea level and the induced height-dependent (local) gravity is derived from the consideration of tidal signals in the ocean and the gravimeter. In combination with the tide gauge time-series, the weakly-non-linear transfer functions can be used to eliminate the Newtonian attraction components by the local water masses from the gravimeter measurements, that is also for non-tidal signals. The corrected gravimetric time-series contain large-scale signatures of ocean loading, predominantly stemming from regional scales and longer, and serve as a proxy for the respective regional sea level.

4 RESULTS

4.1 Comparison of OTL gravity from gravimetry and FES2014b

To corroborate the motivation for a detailed modelling of the height-dependent gravity component, initial results for OTL gravity parameters from both gravimeter time-series are shown for the eight major diurnal and semidiurnal waves in Fig. 7(a) along with the corresponding FES2014b results at AWI and JKS at their individual elevations of $H_0 = 2.31$ m and 41.35 m, respectively, calculated by the OTL provider. Without special consideration of the sea mass variations in the direct vicinities of the gravimeter sites, large differences show up. The largest wave M_2 shows an amplitude of 30 nm s^{-2} from iGrav 047 at AWI, while an amplitude of 56 nm s^{-2} is observed by gPhoneX 152 at JKS. These figures show the different proportions of the direct Newtonian attraction effects from the local sea masses on both gravimeters due to their different elevations and locations. FES2014b provides OTL gravity amplitudes of 14 and 181 nm s^{-2}, respectively, showing inconsistencies due to the insufficient land-sea mask with regard to the small island of Heligoland.

By applying the empirical transfer functions from Table 2 and Fig. 5 on the iGrav 047 (AWI) and gPhoneX 152 (JKS) time-series, the height-independent OTL gravity parameters can be separated and are shown for the eight major diurnal and semidiurnal waves as phasor plots in Fig. 7(b) and numerically in Table A1. In addition, the OTL gravity parameters from FES2014b are shown for AWI at $H_0 = 0$ m. By comparison of Figs 7(a) and (b), it is first obvious that the OTL height-dependent gravity signals are much larger than the OTL height-independent signals by factors up to 10 (see also Fig. 6). The two resulting height-independent gravimetric time-series provide very similar OTL parameters with amplitudes between 0.3 nm s^{-2} (Q_1) and 11 nm s^{-2} (M_2) and uncertainties of 0.1–0.2 nm s^{-2} RMSE for iGrav 047 and a factor of 2 worse for gPhoneX 152. The poorer accuracy of gPhoneX 152 results can be explained by the higher noise level of the instrument, the lack of long-term stability and the shorter time-series (1.5 yr gPhoneX 152 versus 2 yr of iGrav 047) as well as the worse quality of the reduction of the height-dependent gravity component.

The OTL height-independent amplitude differences between iGrav 047 (AWI) and gPhoneX 152 (JKS) are between 0.05 nm s^{-2} (Q_1) and 0.6 nm s^{-2} (K_1) with a mean absolute difference of 0.3 nm s^{-2} for the eight major diurnal and semidiurnal waves. The OTL height-independent phase differences are between 1° (N_2) and 28° (Q_1) with a mean absolute difference of 12°. All results confirm the uncertainty estimations. These results show the efficiency of the empirical modelling presented in Section 3.3 for the reduction of the OTL height-dependent gravity effects, which allows the remarkable statement that the site selection of the gravimeters on the island of Heligoland does not affect the results of the OTL height-independent gravity parameters at the level of a few 0.1 nm s^{-2}. Even more, this accuracy is expected to improve with continuation of the iGrav time-series.

The OTL height-independent amplitude differences between the gravimeter time-series and FES2014b at $H_0 = 0$ m are between 0.0 nm s^{-2} (M_2) and 0.9 nm s^{-2} (O_1 and S_2) for iGrav 047 (AWI) with a mean absolute difference of 0.4 nm s^{-2}. For gPhoneX 152 (JKS), the differences to FES2014b at $H_0 = 0$ m are between 0.1 nm s^{-2} (Q_1) and 1.4 nm s^{-2} (K_1 and O_1) and the mean absolute difference is 0.7 nm s^{-2}. The mean absolute OTL height-independent phase differences between iGrav 047 (AWI) and FES2014b as well as gPhoneX 152 (JKS) and FES2014b are 22° and 27°, respectively. The differences between the gravimeter time-series and FES2014b are largest for the O_1 wave with 72° and 61° and exceed the uncertainty estimations from the gravimeter time-series, indicating deficiencies in FES2014b for this particular tide in the North Sea. The fact that the overall differences are significantly less between the gravimetric time-series than to FES2014b implies that additional uncertainties at the level of a few 0.1 nm s^{-2} reside in either the FES2014b hydrodynamic ocean tide model or the model-based OTL computations.

The overall accuracy of separating the OTL height-dependent and height-independent signals in both gravimeter time-series can be estimated by the gravity differences between the two gravimeter time-series after the reduction of the height-dependent component. These include residual OTL height-dependent signals from the imperfect empirical modelling and OTL height-independent differences which add up with different phases. Fig. 8(a) shows the corresponding gravity differences without any reduction of tides and atmospheric effects between iGrav 047 (AWI) and gPhoneX 152 (JKS). The significant reduction of scatter invoked by the reduction of the height-dependent gravity contribution clearly underlines the value of the presented method. Differences on timescales of a few days and longer between the two gravimeter time-series are visible, but not relevant for the analysis of diurnal and semidiurnal tides in this study. The long-term differences are dominated by the irregular residual gPhoneX 152 drift, which cannot be fully eliminated, while differences in the hydrological signals at the two gravimeter sites, that is during precipitation events, are at the level of 5 nm s^{-2} and below. Finally, the gap in the gPhoneX 152 data from 27 June to 6 July 2020 shows up.

Figs 8(b) and (c) show the PSD and power spectrum estimates, respectively, for the gravity differences between iGrav 047 (AWI) and gPhoneX 152 (JKS). From the PSD estimates, the strong signal reduction in the tidal band is evident with the semidiurnal band showing a stronger reduction than the diurnal band. Similarly, a significant reduction for the 1/4-diurnal tides is observed, while the 1/6-diurnal spectrum retains more signal, which is expected due to neglecting $r = 3$ and higher contributions in the transfer functions. The power spectra are calculated by scaling each estimate of the PSD by the equivalent noise bandwidth of the applied
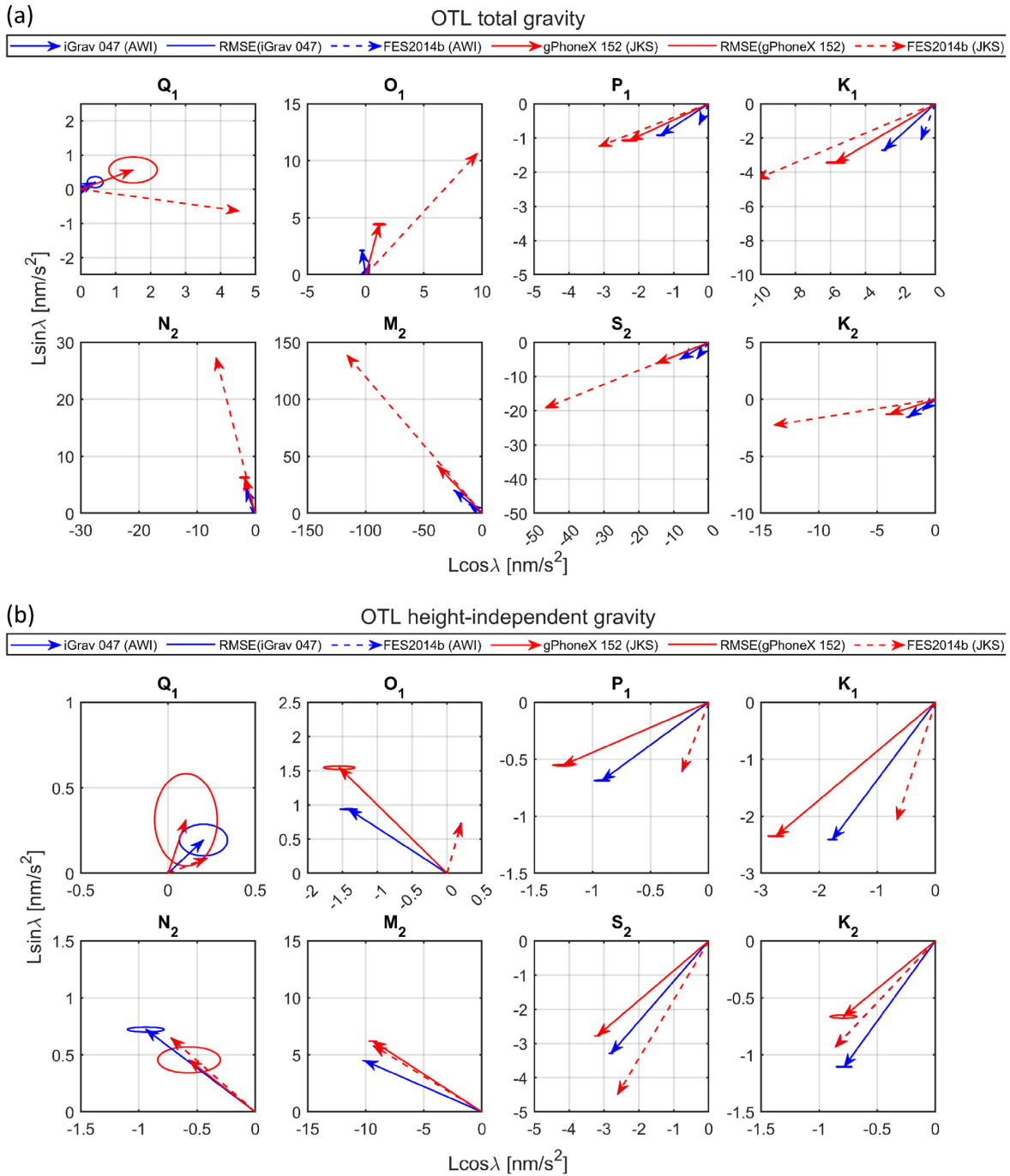
Figure 7. Phasor plots with OTL results for total (a) and height-independent (b) gravity signals from iGrav 047 at AWI (solid blue) and gPhoneX 152 at JKS (solid red) both including RMSE as well as corresponding values from the Ocean tide loading provider (dashed blue and red, respectively, identical for height-independent signals, height-independent gravity evaluated at $H_0 = 0$ m). Please note the differences in axis scaling up to factor 30.

Hamming window and provide the estimates of the power at each frequency. The power estimates are largest for K_1 and M_2 but do not exceed $0.5\ \mathrm{nm\,s^{-2}}$ in both cases for the height-independent gravity differences. The overall weaker reduction of the diurnal tides is certainly related to the NDFW resonance of the Earth tides, a reduced accuracy of the ocean tide models in the North Sea due to smaller amplitudes, and to the fact that these are not considered in the fitting process for the empirical transfer functions. There may be a frequency dependence of the transfer functions, which has not

been investigated so far. The semidiurnal tide S_2 is a special case due to atmospheric impacts which can cause larger discrepancies. Generally, the height-independent effects from Section 3.3 and this section are calculated slightly different which could induce small discrepancies. However, the maximum difference of $0.5\ \mathrm{nm\,s^{-2}}$ in M_2 with an observed amplitude of $288\ \mathrm{nm\,s^{-2}}$ also confirms the absence of systematic errors larger than 0.2 per cent, that is primarily errors in the amplitude calibration of both iGrav 047 and gPhoneX 152.
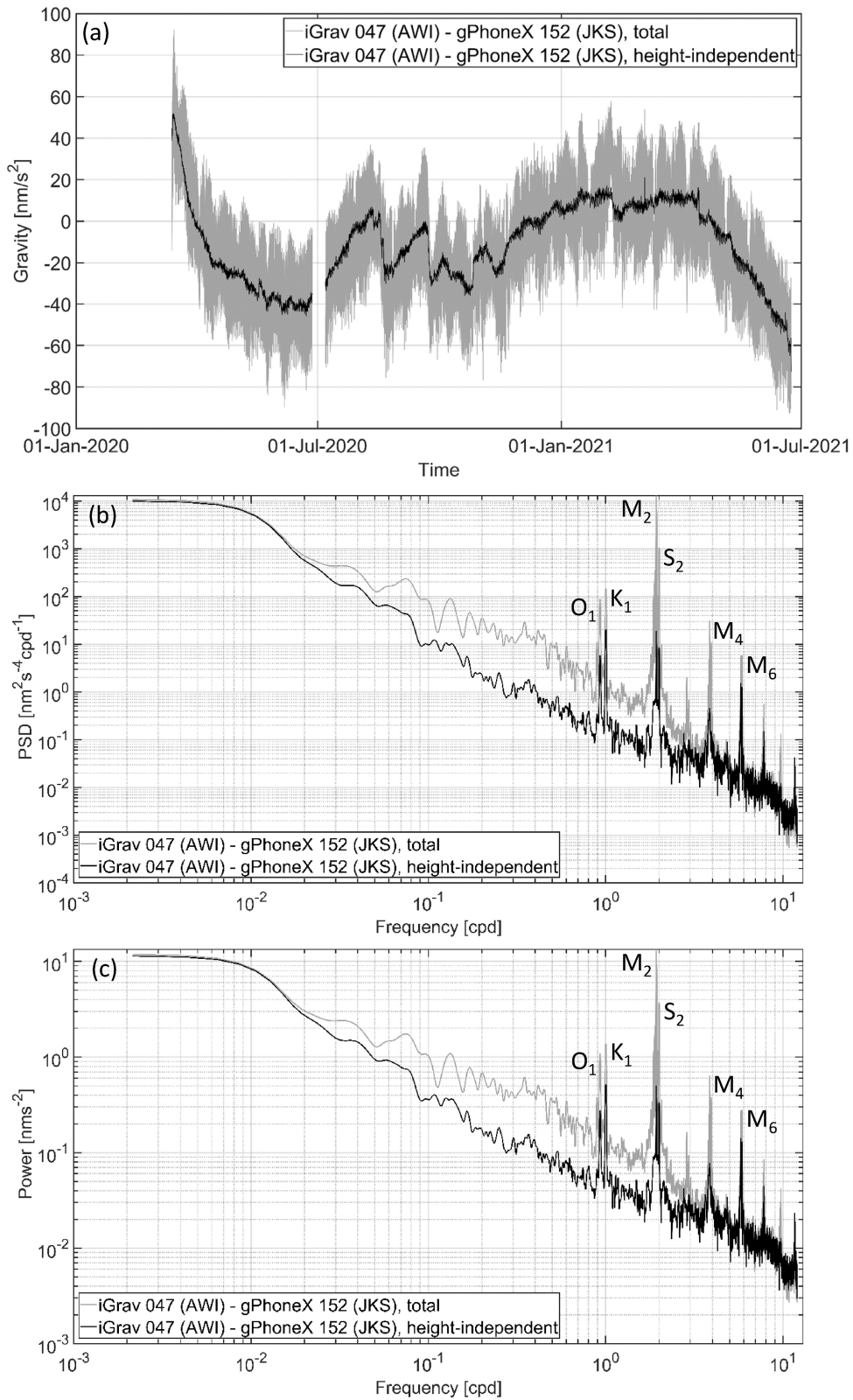
Figure 8. Time-series (a), PSD (b) and power spectrum (c) of gravity differences between iGrav 047 at AWI and gPhoneX 152 at JKS before (grey) and after (black) reduction of the height-dependent gravity component by empirical transfer functions from Table 2.

4.2 Comparison of OTL vertical displacements from gravimetry, GNSS and FES2014b

The high accuracy, long-term stability and high temporal resolution of iGrav 047 at AWI are very beneficial for tidal and non-tidal ocean loading analysis not only in terms of height-independent gravity but potentially also in terms of vertical displacements, as these dominate the height-independent gravity signals with both functionals being insensitive to local mass variations and the shoreline. This is clearly shown by the comparison of the OTL in-phase (a and c) and the quadrature terms (b and d) in Fig. 9 exemplarily for the M_2 tidal wave. Of course, the direct estimation of OTL vertical displacements from GNSS observations is generally preferable to an approximate solution from gravimetry. However, there are situations where GNSS data are not available, the high-accuracy GNSS evaluation/processing (e.g. according to Penna *et al.* 2015) is difficult or estimates completely independent of GNSS are requested. In addition, this solution would improve the efficiency and flexibility of gravimetry by reducing the need for GNSS. Therefore, the gravimetry-based determination of OTL vertical displacements with target uncertainties of a few 0.1 mm is exploited as by-product of this primarily gravimetric study.

The OTL vertical displacements from iGrav 047 (AWI) are provided including uncertainty estimates to be compared with GNSS and FES2014b. The required transfer between OTL height-independent gravity and vertical displacements is done by individual FES2014b-based height-to-gravity ratios dh/dg and phase shifts $dg - dh$ for the eight major diurnal and semidiurnal waves (e.g. de Linage *et al.* 2009). It should be noted that OTL vertical displacements do not include a height-dependent component and are not sensitive to the local shoreline. The dh/dg ratios are approximately 1 mm $(\mathrm{nm\,s^{-2}})^{-1}$ for the diurnal waves with the exception of O_1 (see previous section) and 0.5 mm $(\mathrm{nm\,s^{-2}})^{-1}$ for the semidiurnal waves (Table A2), while the phase shifts differ largely for the diurnal waves and are around $0°$ for the semidiurnal waves. For the validity of this approach, it is crucial to analyse the lateral variability of the height-to-gravity ratios and phase shifts within the North Sea. Fig. 10 shows the corresponding variations relative to the values at the island of Heligoland for the largest diurnal and semidiurnal tidal waves K_1 and M_2, respectively. While the signature of the K1 parameters is very stable, Heligoland is located approximately 100 km away from a M_2 double amphidrome, which limits the regional validity of this approach in the German Bight to a certain extent. However, it should be noted that this is a rather rare case. In the surroundings of $1°$ in both latitude and longitude from Heligoland, the M_2 variations of the ratios and phase shifts relative to Heligoland remain within 10 per cent (0.9–1.1 in Fig. 10) and $\pm 5°$, respectively. According to the numbers in Tables A2 and A3, these ratio variabilities affect the OTL vertical displacements of M_2 from this approach by 0.5 mm in amplitude within the region of interest. Larger variabilities of the height-to-gravity ratios can thus limit the solution in coastal study areas. The uncertainties of the height-to-gravity ratios are estimated from the differences between corresponding OTL parameters at the island of Heligoland with an altitude of $H_0 = 0$ m from five global ocean tide models, that is FES2014b, EOT20, TPXO9.5a, GOT4.10c and HAMTIDE. The standard deviations of the height-to-gravity ratios are between 0.2 and 0.4 mm $(\mathrm{nm\,s^{-2}})^{-1}$ for the diurnal waves and 0.01–0.09 mm $(\mathrm{nm\,s^{-2}})^{-1}$ for the semidiurnal waves. The better agreement of the semidiurnal tides in this area, that is a smaller ensemble spread, can be explained to large part by the larger amplitudes.
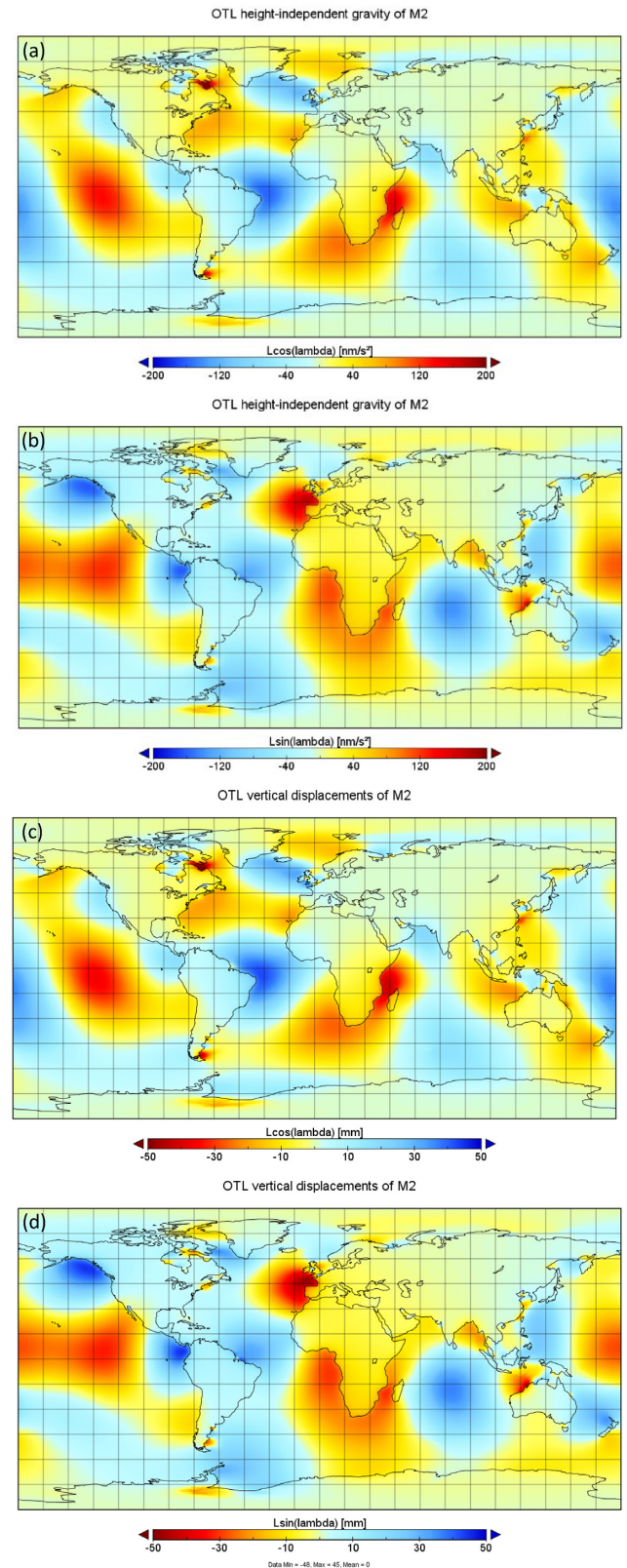

Figure 9. OTL in-phase and quadrature components of M2 from FES2014b for height-independent gravity (a and b) and for vertical displacements (c and d).
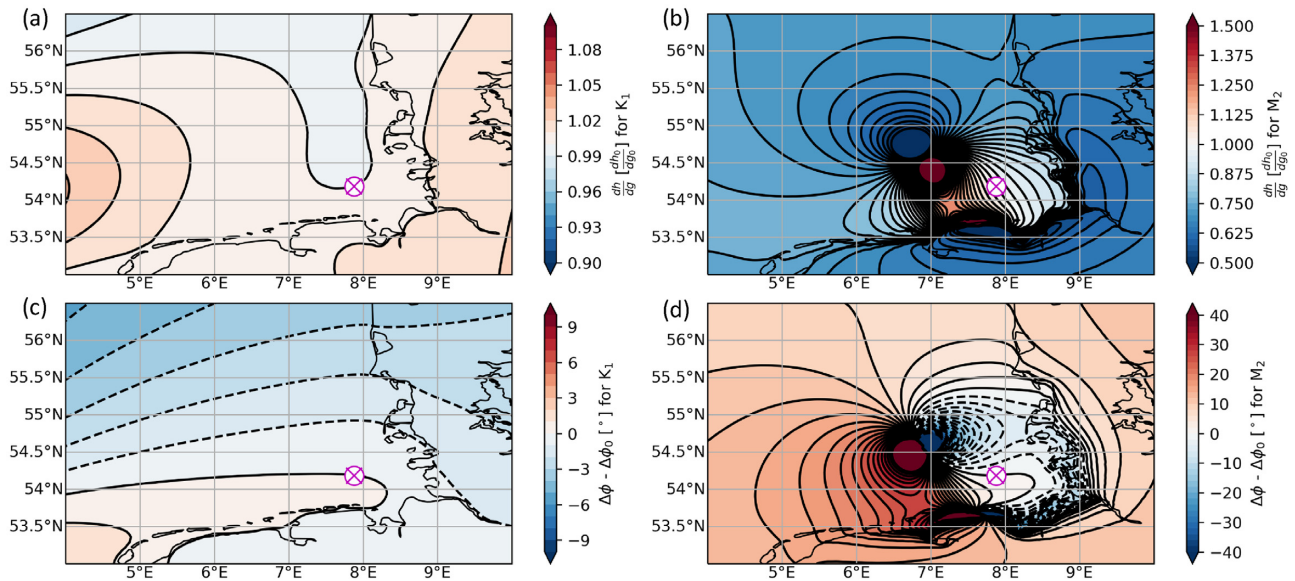
Figure 10. Height-to-gravity ratios dh/dg (a) and (b) as well as phase shifts $dg - dh$ (c) and (d) from the OTL height-independent gravity and vertical displacements of the tidal waves K_1 and M_2, respectively, based on FES2014b relative to the numbers at Heligoland (magenta cross) provided in Table A2.
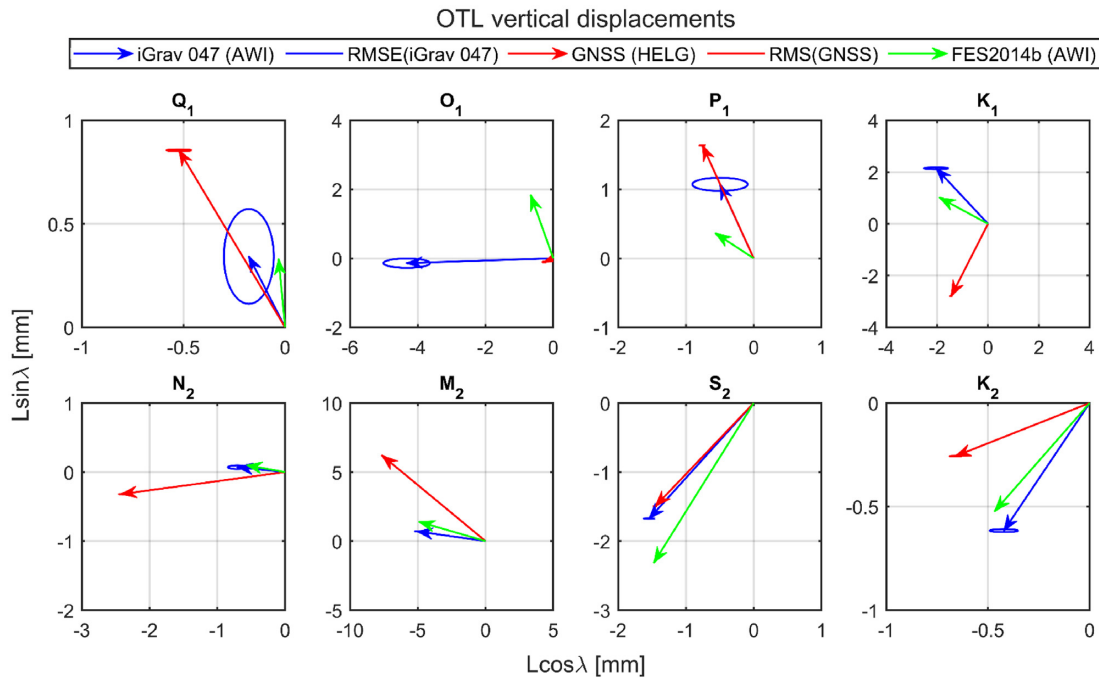

Figure 11. Phasor plots with OTL vertical displacements from iGrav 047 height-independent gravity converted by $\dot{h}/\dot{g}$ factors and corresponding phase shifts from FES2014b (blue), GNSS station HELG (red) and FES2014b (green) via Ocean tide loading provider; vertical displacements with centre-of-mass corrections (CMC) which means that these refer to the joint mass centre of solid Earth and ocean. Please note the differences in axis scaling up to factor 15.

Table A3 shows the resulting vertical displacements from the combined iGrav 047-FES2014b approach. The RMSE for the diurnal waves are 0.3–0.7 mm and 5–52° in terms of amplitudes and phases, respectively, and do not fully meet the expectations caused by significant discrepancies between recent models. The semidiurnal waves, however, fully meet the initial target of a few 0.1 mm uncertainty with RMSE for the amplitudes between 0.07 mm (K_2) and 0.16 mm (M_2) and RMSE for the phases between 1° (M_2) and 11° (N_2). With these results, it is now possible to evaluate independently and with superior accuracy (at least for the semidiurnal

waves) the OTL vertical displacements estimated from tidal analysis of the GNSS time-series. As HELG and HEL2 provide very similar OTL parameters with insignificant differences of 0.001 mm and 0.00° only, the results of HELG are shown. Fig. 11 depicts the OTL vertical displacement parameters for the eight major diurnal and semidiurnal waves as phasor plots from the combined iGrav 047-FES2014b approach, from GNSS station HELG and directly from FES2014b. The differences between the combined iGrav 047-FES2014b approach and FES2014b are between 0.0 (M_2) and 0.8 mm (K_1) with a mean absolute difference of 0.3 mm

meeting the uncertainty estimations and the initial uncertainty target of a few 0.1 mm. However, this comparison excludes the O_1 results which are suspected to be erroneous with an amplitude difference of 2.4 mm and a phase difference of 72° (see also Section 4.1).

The comparisons with the GNSS results from station HELG are significantly worse with a mean absolute difference of 1.3 mm and significant amplitude differences up to 6 mm (M_2) compared to both iGrav 047 and FES2014b vertical displacements. These differences easily exceed the formal uncertainty estimates from the tidal analysis of almost 5 yr of GNSS data at the level of 0.1 mm in OTL amplitudes and a few degrees in OTL phases (RMSE) suggesting systematic effects included in the estimation of OTL vertical displacements from GNSS, especially residual day boundary jumps in the GNSS solution (Section 2) affecting the tidal analysis with ET34-X-V80. So the initial target uncertainty for the OTL vertical displacements of a few 0.1 mm cannot be confirmed with GNSS data as expected from recent studies (Penna *et al.* 2015).

5 CONCLUSIONS

The small offshore island of Heligoland in the North Sea is used as study area for the setup of a terrestrial gravity gradiometer approach including iGrav 047 at an elevation of 2 m above mean sea level and gPhoneX 152 at 41 m with a horizontal distance of 800 m. The largest differences between the two gravimeter time-series arise from the direct Newtonian attraction of the local sea masses. Empirical transfer functions between the local sea level from a nearby tide gauge and height-dependent attraction effects are estimated and reduced from the two gravimeter sites.

The two resulting height-independent gravimetric time-series provide very similar OTL parameters with mean absolute amplitude differences of 0.3 nm s^{-2} for the eight major diurnal and semidiurnal waves. These numbers confirm well the uncertainty estimates of 0.1–0.2 nm s^{-2} from the tidal analysis of the iGrav 047 time-series and the factor of 2 worse from the gPhoneX 152 time-series. The OTL height-independent parameters from the gravimeter time-series are also compared with corresponding values from FES2014b at an elevation of $H_0 = 0$ m providing mean absolute amplitude differences of 0.4 nm s^{-2} (iGrav 047) and 0.7 nm s^{-2} (gPhoneX 152) suggesting again a poorer accuracy of the gPhoneX 152 time-series and residual model deficits in FES2014b.

As by-product of this study, the transition from OTL height-independent gravity to vertical displacements is done by individual model-based height-to-gravity ratios and phase shifts for the eight major diurnal and semidiurnal waves from FES2014b. The estimated uncertainty of the OTL vertical displacements from this combined iGrav-FES2014b based approach is 0.3–0.7 mm for the diurnal waves and 0.1–0.2 mm for the semidiurnal waves. While the differences of the OTL vertical displacements from this combined approach and FES2014b confirm these uncertainty estimates revealing a mean absolute amplitude difference of 0.3 mm, the results from the GNSS station HELG are significantly larger with a mean absolute amplitude difference of 1.3 mm including amplitude differences of up to 6 mm (M2). These numbers suggest systematic effects included in the estimation of OTL vertical displacements from GNSS.

Overall, this study shows that it is possible to provide regionally representative OTL parameters from a 2-yr-record of the iGrav 047 superconducting gravimeter at the island of Heligoland by empirical modelling of the direct Newtonian effects from the sea masses with

an uncertainty of a few 0.1 nm s^{-2} and 0.1 mm in terms of height-dependent gravity and vertical displacements, respectively. This accuracy will further improve with the ongoing extension of the time-series. An improved estimation of the loading effects from non-linear shallow water tides and the degree-3 tidal waves are expected. The analysis of annual variations of the OTL parameters is planned on the basis of a multiyear iGrav time-series. The spectral data from the local permanent network of six broad-band seismometers will be compared with the iGrav 047 at AWI focusing on local microseism in the North Sea and its temporal modulation.

Besides the extended analysis of OTL parameters, future work will be devoted to non-tidal ocean loading, especially the analysis of storm surge signals in the North Sea during winter periods. The empirical transfer functions from this study do not only apply to tidal but also to non-tidal effects and are thus, together with the OTL analyses, the essential prerequisites for the study of regionally representative non-tidal height-independent ocean loading signals. The results are expected to be used for the calibration and validation of satellite gravimetry from GRACE Follow-On and corresponding de-aliasing products AOD1B RL06 as well as the reduction of planned optical clock measurements at the level of 10^{-18} for the height transfer between the mainland and the island of Heligoland.

DATA AVAILABILITY

All datasets used within this study are publicly available. Gravity and barometric pressure data from the gravimeters iGrav 047 at AWI and gPhoneX 152 at JKS are operated by GFZ and are available from the IGETS database hosted by the Information System and Data Center at GFZ (https://doi.org/10.2312/gfz.b103-16087; Voigt *et al.* 2016b). The sea level heights from the tide gauges HELBH and HELSH are operated by WSV. Data of the past 30 d are available from WSV (2022), while long time-series are available upon request from BfG (2022). The GNSS stations HELG and HEL2 are operated by BKG and part of the EUREF and GREF network, respectively. Raw GNSS data are available from BKG (2022), while processed data are published by Deng (2023).

REFERENCES

Agnew, D., 2007. Earth tides, in *Treatise on Geophysics,* 1st edn, Vol. 3: Geodesy, pp. 163–195, ed. Herring, T., Elsevier.

Agnew, D.C. 2013. SPOTL: some programs for ocean-tide loading, Scripps Institution of Oceanography Technical Report, University of California, Available at: https://igppweb.ucsd.edu/~agnew/Spotl/spotlmain.html, accessed 28 July 2022.

Baker, T.F. & Bos, M.S., 2003. Validating Earth and ocean tide models using tidal gravity measurements, *Geophys. J. Int.,* **152,** 468–485.

Becker, D., Cristiano, L., Peikert, J., Kruse, T., Dethof, F., Hadziioannou, C. & Meier, T., 2020. Temporal modulation of the local microseism in the North Sea, *J. geophys. Res.,* **125**(10), e2020JB019770, doi:10.1029/2020JB019770.

BfG, 2022. Datenstelle der Bundesanstalt für Gewässerkunde. Email: Datenstelle-M1@bafg.de.

BKG, 2022. The BKG GNSS Data Center, Available at: https://igs.bkg.bund.de/, accessed 27 July 2022.

Bos, M.S. & Scherneck, H.-G., 2022. The free ocean tide loading provider, Available at: http://holt.oso.chalmers.se/loading/, accessed 28 July 2022.

Bos, M.S., Baker, T.F., Røthing, K. & Plag, H.-P., 2002. Testing ocean tide models in the Nordic seas with tidal gravity observations, *Geophys. J. Int.,* **150,** 687–694.

Boy, J.-P., Llubes, M., Hinderer, J. & Florsch, N., 2003. A comparison of tidal ocean loading models using superconducting gravimeter data, *J. geophys. Res.,* **108**(B4), 2193. doi:10.1029/2002JB002050.

Boy, J.-P. & Lyard, F., 2008. High-frequency non-tidal ocean loading effects on surface gravity measurements, *Geophys. J. Int.,* **175,** 35–45.

Boy, J.-P., Barriot, J.-P., Förste, C., Voigt, C. & Wziontek, H., 2020. Achievements of the first 4 years of the International Geodynamics and Earth Tide Service (IGETS) 2015–2019, in *Beyond 100: The Next Century in Geodesy. International Association of Geodesy Symposia,* Vol. **152,** eds Freymueller, J.T. & Sánchez, L., Springer.

Carriére, S.D. *et al.*, 2021. First evidence of correlation between evapotranspiration and gravity at a daily time scale from two vertically spaced superconducting gravimeters, *Geophys. Res. Lett.,* **48**(24), e2021GL096579. doi:10.1029/2021GL096579.

Crossley, D. *et al.*, 1999. Network of superconducting gravimeters benefits several disciplines. *EOS, Trans. Am. geophys. Un.,* **80,** 121–126.

Dehant, V., Defraigne, P. & Wahr, J.M, 1999. Tides for a convective Earth, *J. geophys. Res.,* **104,** 1035–1058.

Deng, Z., 2023. Heligoland GNSS hourly time series positioning for 2017-2021, GFZ Data Services.

Deng, Z., Gendt, G. & Schöne, T., 2015. Status of the IGS-TIGA Tide Gauge Data Reprocessing at GFZ, in *IAG 150 Years. International Association of Geodesy Symposia,* Vol. **143,** eds Rizos, C. & Willis, P., Springer.

Dobslaw, H., Bergmann-Wolf, I., Dill, R., Poropat, L., Thomas, M., Dahle, C., Esselborn, S., König, R. & Flechtner, F., 2017. A new high-resolution model of non-tidal atmosphere and ocean mass variability for de-aliasing of satellite gravity observations: AOD1B RL06, *Geophys. J. Int.,* **211**(1), 263–269.

Ducarme, B. & Kääriäinen, J., 1980. *The Finnish Tidal Gravity Registrations in Fennoscandia,* Publications of the Finnish Geodetic Institute, 43 pp.

Ducarme, B. & Schueller, K., 2019. Canonical wave grouping as the key to optimal tidal analysis, *Bulletin d'Information des Marées Terr.,* **150,** 12131–12244, http://igets.u-strasbg.fr/BIM/bim150.pdf.

Egbert, G.D. & Erofeeva, S.Y, 2002. Efficient inverse modeling of barotropic ocean tides, *J. Atmos. Oceanic Technol.,* **19**(2), 183–204.

Farrell, W.E., 1972. Deformation of the Earth by surface loads, *Rev. Geophys. Space Phys.,* **10,** 761–797.

Fratepietro, F., Baker, T.F., Williams, S.D.P. & Van Camp, M., 2006. Ocean loading deformations caused by storm surges on the northwest European shelf, *Geophys. Res. Lett.,* **33**(6), L06317. doi:10.1029/2005GL025475.

Goto, H., Sugihara, M., Nishi, Y. & Ikeda, H., 2021. Simultaneous gravity measurements using two superconducting gravimeters to observe temporal gravity changes below the nm s−2 level: ocean tide loading differences at different distances from the coast, *Geophys. J. Int.,* **227**(3), 1591–1601.

Hart-Davis, M.G., Piccioni, G., Dettmering, D., Schwatke, C., Passaro, M. & seitz, F., 2021. EOT20: a global ocean tide model from multi-mission satellite altimetry, *Earth Syst. Sci. Data,* **13,** 3869–3884.

Hartmann, T. & Wenzel, H.-G., 1995. The HW95 tidal potential catalogue. *Geophys. Res. Lett.,* **22**(24), 3553–3556.

Hinderer, J., Crossley, D. & Warburton, R., 2015. Superconducting gravimetry, in *Treatise on Geophysics,* 2nd edn, Vol. **3,** pp. 59–115, ed. Schubert, G., Elsevier.

Jentzsch, G., 1997. Earth tides and ocean tidal loading, in *Tidal Phenomena – Lecture Notes in Earth Sciences,* Vol. **66,** pp. 145–171, eds Wilhelm, H., Zürn, W. & Wenzel, H.-G., Springer.

Kennedy, J., Ferré, T.P.A., Güntner, A., Abe, M. & Creutzfeldt, B., 2014. Direct measurement of subsurface mass change using the variable baseline gravity gradient method, *Geophys. Res. Lett.,* **41** , 2827–2834.

Landerer, F.W. *et al.*, 2020. Extending the global mass change data record: GRACE follow-on instrument and science data performance, *Geophys. Res. Lett.,* **47**(12), e2020GL088306.

de Linage, C., Hinderer, J. & Boy, J.-P., 2009. Variability of the gravity-to-height ratio due to surface loads, *Pure appl. Geophys.,* **166,** 1217–1245.

Lyard, F.H., Allain, D.J., Cancet, M., Carrière, L. & Picot, N., 2021. FES2014 global ocean tide atlas: design and performance, *Ocean Sci.,* **17,** 615–649.

Lysaker, D.I., Breili, K. & Pettersen, B.R., 2008. The gravitational effect of ocean tide loading at high latitude coastal stations in Norway, *J. Geod.,* **82,** 569–583.

Matsumoto, K., Sato, T., Takanezawa, T. & Ooe, M., 2001. GOTIC2: a program for computation of oceanic tidal loading effect, *J. Geod. Soc. Jpn.,* **47,** 243–248.

Merriam, J.B., 1980. The series computation of the gravitational perturbation due to an ocean tide, *Phys. Earth planet. Inter.,* **23,** 81–86.

Neumeyer, J., del Pino, J., Dierks, O., Sun, H.P. & Pflug, H., 2005. Improvement of ocean loading correction on gravity data with additional tide gauge measurements, *J. Geodyn.,* **40,** 104–111.

Olsson, P.A., Scherneck, H.-G. & Ågren, J, 2009. Effects on gravity from non-tidal sea level variations in the Baltic Sea, *J. Geodyn.,* **48**(3–5), 151–156.

Penna, N.T., Bos, M.S., Baker, T.F. & Scherneck, H.-G., 2008. Assessing the accuracy of predicted ocean tide loading displacement values, *J. Geod.,* **82,** 893–907.

Penna, N.T., Clarke, P.J., Bos, M.S. & Baker, T.F., 2015. Ocean tide loading displacements in western Europe: 1. Validation of kinematic GPS estimates, *J. geophys. Res.,* **120,** 6523–6539.

Ray, R.D., 2013. Precise comparisons of bottom-pressure and altimetric ocean tides, *J. geophys. Res.,* **118,** 4570–4584.

Rebischung, P., Altamimi, Z., Ray, J. & Garayt, B., 2016. The IGS contribution to ITRF2014, *J. Geod.,* **90,** 611–630.

Schueller, K., 2015. Theoretical basis for earth tide analysis with the new ETERNA34-ANA-V4.0 program, *Bulletin d'Information des Marées Terr*., **149,** 12 024–12 061.

Schueller, K., 2020. Program SystemETERNA-x et34-x-v80 for Earth and Ocean Tides Analysis and prediction, documentation manual 01: theory and 02: users guide. Technical reports, Institution: http://ggp.bkg.bund.de/eterna?download=7283

Sulzbach, R. *et al.*, 2022. Modeling gravimetric signatures of third-degree ocean tides and their detection in superconducting gravimeter records, . (2022).

Taguchi, E., Stammer, D. & Zahel, W., 2014. Inferring deep ocean tidal energy dissipation from the global high-resolution data-assimilative HAMTIDE model, *J. geophys. Res.,* **119,** 4573–4592.

Timmen, L., 2020. *Absolute gravity measurements at the iGrav 047 site on Helgoland (GFZ Potsdam, AWI facility) with the Hannover gravity meter FG5X-220 in July 2020,* Leibniz Universität Hannover Institutional Repository.

Timmen, L., Rothleitner, C., Reich, M., Schröder, S. & Cieslack, M., 2020. Investigation of Scintrex CG-6 gravimeters in the Gravity Meter

calibration system Hannover, *AVN Allgemeine Vermessungsnachrichten,* **127**(4), 155–162.

Timmen, L., 2021. *Absolute gravity measurements at the iGrav 047 site on Helgoland (GFZ Potsdam, AWI facility) with the Hannover gravity meter FG5X-220 in June 2021,* Leibniz Universität Hannover Institutional Repository.

Timmen, L., Gerlach, C., Rehm, T., Völksen, C. & Voigt, C., 2021. Geodetic-gravimetric monitoring of mountain uplift and hydrological variations at Zugspitze and Wank Mountains (Bavarian Alps, Germany), *Remote Sens.,* **13**, 918.

Torge, W. & Müller, J., 2012. *Geodesy,* 4th edn, de Gruyter.

Van Camp, M., de Viron, O., Watlet, A., Meurers, B., Francis, O. & Caudron, C., 2017. Geophysics from terrestrial time-variable gravity measurements, *Rev. Geophys.,* **55**, 938–992.

Voigt, C, Denker, H. & Timmen, L., 2016a. Time-variable gravity potential components for optical clock comparisons and the definition of international time scales, *Metrologia,* **53**, 1365–1383.

Voigt, C. *et al.*, 2016b. Report on the data base of the international geodynamics and earth tide service (IGETS), Scientific technical report STR Potsdam, GFZ German Research Centre for Geosciences [data set], Potsdam, Germany.

Voigt, C., Stolarczuk, N., Pflug, H., Förste, C., Flechtner, F., Peters, H. & Fietz, M., 2020. *Superconducting Gravimeter Data from Helgoland – Level 1,* GFZ Data Services.

Voigt, C. *et al.*, 2021. Technical note: introduction of a superconducting gravimeter as novel hydrological sensor for the Alpine research catchment Zugspitze, *Hydrol. Earth Syst. Sci.,* **25**, 5047–5064.

Weise, A., Timmen, L., Deng, Z., Gabriel, G., Rothleitner, C., Schilling, M. & Voigt, C., 2020. Observing ocean mass variability with spring gravimeters – storm surge induced signals on the North Sea island Helgoland, *AVN Allgemeine Vermessungsnachrichten,* **127**(4), 163–173.

Welch, P.D., 1967. The use of fast fourier transform for the estimation of power spectra: a method based on time averaging over short, modified periodograms, *IEEE Trans. Audio Electroacoust.,* **15**(2), 70–73.

Wessel, P. & Smith, F., 1998. New, improved version of generic mapping tools released, *EOS, Trans. Am. geophys. Un.,* **79**, 579.

Wilmes, H., Wziontek, H., Falk, R. & Bonvalot, S. 2009. AGrav – The New International Absolute Gravity Database of BGI and BKG and its benefit for the Global Geodynamics Project (GGP), *J. Geodyn.,* **48**, 305–309.

WSV, 2022. Wasserstraßen- und Schifffahrtsverwaltung des Bundes Pegelonline. Aviable at: https://www.pegelonline.wsv.de/webservices/files/Wasserstand+Rohdaten/NORDSEE, accessed 16 June 2022.

Yuan, L. & Chao, B.F., 2012. Analysis of tidal signals in surface displacement measured by a dense continuous GPS array, *Earth planet. Sci. Lett.,* **355-356**, 255–261.

Yuan, L., Chao, B.F., Ding, X. & Zhong, P., 2013. The tidal displacement field at Earth's surface determined using global GPS observations, *J. geophys. Res.,* **118**, 2618–2632.

APPENDIX

Table A1. OTL height-independent gravity amplitudes and phases from iGrav 047 at AWI, gPhoneX 152 at JKS and FES2014b at AWI with $H_0 = 0$ m according to Fig. 7(b).

Tidal wave	iGrav 047		gPhoneX 152		FES2014b	
	Amplitude (RMSE) [nm s^{-2}]	Greenwich phase (RMSE) [°]	Amplitude (RMSE) [nm s^{-2}]	Greenwich phase (RMSE) [°]	Amplitude [nm s^{-2}]	Greenwich phase [°]
Q_1	0.28 (0.17)	43.7 (33.8)	0.33 (0.32)	71.9 (56.4)	0.24	21.7
O_1	1.70 (0.12)	146.5 (4.2)	2.18 (0.22)	135.1 (5.9)	0.76	74.6
P_1	1.14 (0.07)	− 143.2 (3.4)	1.37 (0.09)	− 156.1 (3.8)	0.65	− 110.8
K_1	2.99 (0.08)	− 126.3 (1.5)	3.61 (0.14)	− 139.3 (2.2)	2.17	− 107.8
N_2	1.19 (0.16)	142.5 (7.7)	0.73 (0.29)	141.6 (23.0)	0.97	138.2
M_2	11.04 (0.15)	156.1 (0.8)	11.24 (0.34)	146.7 (1.7)	11.03	148.1
S_2	4.32 (0.06)	− 130.4 (0.8)	4.23 (0.09)	− 138.8 (1.2)	5.20	− 120.2
K_2	1.36 (0.07)	− 125.4 (2.8)	1.03 (0.12)	− 139.7 (6.5)	1.27	− 132.8

Table A2. OTL amplitude and phase relations at AWI with $H_0 = 0$ m from FES2014b via Ocean tide loading provider including single standard deviations (Std) from deviations between 5 recent ocean tide models (FES2014b, EOT20, TPXO9.5a, GOT4.10c and HAMTIDE); vertical displacements with centre-of-mass corrections (CMC) which means that these refers to the joint mass centre of solid earth and ocean.

Tidal wave	Height-independent gravity dg		Vertical displacements dh		Vertical displacement-gravity ratios	
	Amplitude [nm s^{-2}]	Greenwich phase [°]	Amplitude [mm]	Greenwich phase [°]	Amplitude (Std) dh/dg [mm (nm s^{-2})$^{-1}$]	Greenwich phase (Std)dg − dh [°]
Q_1	0.24	21.7	0.33	95.5	1.375 (0.433)	− 73.8 (51.7)
O_1	0.76	74.6	1.94	110.0	2.553 (0.369)	− 35.4 (10.3)
P_1	0.65	− 110.8	0.67	147.3	1.031 (0.358)	101.9 (12.8)
K_1	2.17	− 107.8	2.15	152.1	0.991 (0.160)	100.1 (4.7)
N_2	0.97	138.2	0.58	170.0	0.598 (0.090)	− 31.8 (8.1)
M_2	11.03	148.1	5.08	164.1	0.461 (0.013)	− 16.0 (1.2)
S_2	5.20	− 120.2	2.74	− 122.5	0.527 (0.017)	2.3 (2.5)
K_2	1.27	− 132.8	0.70	− 131.8	0.551 (0.041)	− 1.0 (5.3)

Table A3. OTL amplitudes and phases from iGrav 047 including root-mean-square-error (RMSE) from tidal analysis from height-independent gravity and from variance propagation for vertical displacements.

Tidal wave	Height-independent gravity dg		Vertical displacements dh	
	Amplitude (RMSE) [nm s^{-2}]	Greenwich phase (RMSE) [°]	Amplitude (RMSE) [mm]	Greenwich phase (RMSE) [°]
Q_1	0.28 (0.17)	43.7 (33.8)	0.39 (0.26)	117.5 (61.8)
O_1	1.70 (0.12)	146.5 (4.2)	4.33 (0.70)	− 178.1 (11.1)
P_1	1.14 (0.07)	− 143.2 (3.4)	1.18 (0.42)	114.9 (13.2)
K_1	2.99 (0.08)	− 126.3 (1.5)	2.96 (0.48)	133.6 (4.9)
N_2	1.19 (0.16)	142.5 (7.7)	0.71 (0.14)	174.3 (11.2)
M_2	11.04 (0.15)	156.1 (0.8)	5.09 (0.16)	172.1 (1.4)
S_2	4.32 (0.06)	− 130.4 (0.8)	2.28 (0.08)	− 132.7 (2.6)
K_2	1.36 (0.07)	− 125.4 (2.8)	0.75 (0.07)	− 124.4 (6.0)